

# OPTOELECTRONICS OF NANOCRYSTALS: INFRARED ABSORBING LEAD HALIDE PEROVSKITE

A Thesis

submitted to  
Indian Institute of Science Education and Research Pune  
in partial fulfilment of the requirements for the  
BS-MS Dual Degree Programme

by

Mayank Goyal



Indian Institute of Science Education and Research Pune

Dr. Homi Bhabha Road,

Pashan, Pune 411008, INDIA.

April, 2020

Supervisor: Emmanuel Lhuillier

© Mayank Goyal 2020

All rights reserved



## CERTIFICATE

This is to certify that this dissertation entitled “**Optoelectronics of Nanocrystals: Infrared Absorbing Lead Halide Perovskite**” towards the partial fulfilment of the BS-MS dual degree programme at the **Indian Institute of Science Education and Research, Pune** represents study/work carried out by **Mayank Goyal** at the **Sorbonne University** under the supervision of **Dr. Emmanuel Lhuillier, Research Scientist, Institut des NanoSciences de Paris (INSP), Sorbonne University** during the academic year 2019-2020.

STUDENT  
**Mayank Goyal**

Handwritten signature of Mayank Goyal, featuring a circled 'M' above the name 'Goyal'.

SUPERVISOR  
**Dr. Emmanuel Lhuillier**

Handwritten signature of Dr. Emmanuel Lhuillier, written in a cursive style.



## DECLARATION

I hereby declare that the matter embodied in the report entitled “**Optoelectronics of Nanocrystals: Infrared Absorbing Lead Halide Perovskite**” are the results of the work carried out by me at the **Institut des NanoSciences de Paris (INSP), Sorbonne University**, under the supervision of **Dr. Emmanuel Lhuillier** and the same has not been submitted elsewhere for any other degree.

STUDENT  
Mayank Goyal

Handwritten signature of Mayank Goyal, featuring a circled 'M' above the name 'Goyal' which is underlined.

SUPERVISOR  
Dr. Emmanuel Lhuillier

Handwritten signature of Dr. Emmanuel Lhuillier, written in a cursive style and underlined.



## **ACKNOWLEDGEMENTS**

Firstly, I would like to thank my supervisor Dr. Emmanuel Lhullier, who not only guided and supported me throughout my project but also constantly motivated me to become a better researcher and a better version of myself. I would like to thank Dr. Angshuman Nag for agreeing to be my co-supervisor and for his guidance at the start of the project and his support during the whole duration. I would like to extend my thanks to Dr. Surjeet Singh who, apart from being a member of my thesis advisory committee, helped develop my interest in nanoelectronics through the course 'Physics at Nanoscale'.

I would like to thank the members of the Optoelectronic Materials group at IISER Pune and the OCN group at INSP for sharing their knowledge to aid me in my project and for making my time in the lab fun and enjoyable. I would like to acknowledge the relevant authorities at IISER Pune and Sorbonne University for providing me with this opportunity. I would also like to acknowledge the Department of Chemistry, IISER Pune; INSP; and the SOLEIL Synchrotron for allowing me to use their facilities. I am grateful to DST INSPIRE, ERASMUS, and INSP for providing financial support.

Lastly, I would like to thank my family and friends. This project would have been impossible without their support and company.



# **Table of Contents**

List of Figures .....	3
List of Tables .....	3
ABSTRACT.....	5
1 INTRODUCTION.....	7
1.1 Nanostructured Semiconductors .....	7
1.2 Halide Perovskites .....	9
1.3 Different Shapes and Compositions of Perovskites Nanocrystals .....	10
1.4 Motivation of this Project .....	11
1.5 Work Undertaken in this Project.....	12
2 MATERIALS AND METHODS .....	15
2.1 Synthesis Methods for FAPI .....	15
2.2 Characterisation of Materials .....	18
2.3 Synthesis Methods for Perovskites and Other Materials .....	19
2.4 Device Fabrication .....	22
2.5 Characterisation of Materials .....	24
2.6 Characterisation of Devices .....	25
2.7 Data Analysis .....	27
3 RESULTS AND DISCUSSION .....	29
3.1 Characterisation of FAPI Nanocrystals Synthesised at IISER Pune.....	29
3.2 Band Gap Tuning Through Size, Shape and Composition of Nanocrystals .....	31
3.3 Charge Transport Properties of FAPI .....	37
3.4 Mixing FAPI and PbS.....	41
3.5 XPS Measurements .....	44
4 CONCLUSION .....	49
4.1 Summary .....	49
4.2 Future Outlook.....	50
REFERENCES .....	51



## **List of Figures**

Figure 1.1: Schematic representation of the quantum confinement effect .....	8
Figure 1.2: The perovskite structure .....	9
Figure 1.3: Structural formula of MA and FA .....	11
Figure 2.1: Scheme of hot injection method used for synthesis .....	16
Figure 2.2: Scheme of fabrication of Au interdigitated electrodes on Si/SiO <sub>2</sub> wafers .....	23
Figure 2.3: Scheme of X-ray photoemission spectroscopy .....	25
Figure 2.4: Scheme of the probe setup.....	26
Figure 3.1: Characterisation of FAPI NCs.....	29
Figure 3.2: pXRD of ‘not’ FAPI NPLs.....	31
Figure 3.3: Absorption spectra- temperature of synthesis .....	32
Figure 3.4: Absorption spectra- synthesis method.....	33
Figure 3.5: Structural representation of L <sub>2</sub> PbX <sub>4</sub> and L <sub>2</sub> [APbX <sub>3</sub> ]PbX <sub>4</sub> .....	34
Figure 3.6: Absorption Spectra- mixed halide.....	34
Figure 3.7: Absorption Spectra- reaction precursor.....	35
Figure 3.8: Microscopic images of films on interdigitated electrodes.....	38
Figure 3.9: I-V curves of FAPI NCs film .....	39
Figure 3.10: Arrhenius plot of photocurrent v/s temperature of the film .....	40
Figure 3.11: TEM images of FAPI NCs, PbS CQDs, and FAPI-PbS hybrid.....	41
Figure 3.12: Absorption spectra of FAPI NCs, PbS CQDs, and FAPI-PbS hybrids.....	42
Figure 3.13: Photocurrent v/s power in films of FAPI-PbS hybrids .....	43
Figure 3.14: Photocurrent spectra of films of FAPI-PbS hybrids.....	44
Figure 3.15: XPS spectra of FAPI NCs, PbS CQDs, and FAPI-PbS hybrid.....	45
Figure 3.16: Band gap structures of FAPI NCs and PbS CQDs.....	46
Figure 3.17: Fitted core level peaks of Pb 4f.....	47

## **List of Tables**

Table 3.1: Absorption of LHPs of different size, shape and composition.....	36
---	----



## **ABSTRACT**

Lead halide perovskites (LHPs) have become increasingly popular as the base material in solar cells and other optoelectronic devices due to their defect tolerant structure leading to high power conversion efficiency and high photoluminescence quantum yield. They are wide band gap materials absorbing and emitting in UV-visible range. Hence, solar cells made from LHPs do not work at full potential as they are unable to absorb the IR part of the solar spectrum. Formamidinium Lead Iodide (FAPbI<sub>3</sub>) has the smallest band gap and relatively high stability among commonly used LHPs. The aim of this thesis is to develop a material using FAPbI<sub>3</sub> that absorbs IR radiation while maintaining the transport properties of lead halide perovskites. This is achieved by doping PbS colloidal quantum dots (CQDs) in FAPbI<sub>3</sub> nanocrystals.

LHPs nanocrystals were synthesised using different methods, and the effect of their size, shape, and composition on the band gap was studied. Characterisation of FAPbI<sub>3</sub> nanocrystals was done to study its structure. Films of FAPbI<sub>3</sub> nanocrystals were deposited on gold interdigitated electrodes, and transport properties were studied. Evidence of trap free band gap of FAPbI<sub>3</sub> was obtained by studying the photocurrent dependence on illumination power and dark current variation with temperature. Lastly, a hybrid material was created by mixing FAPbI<sub>3</sub> nanocrystals and PbS CQDs. By studying the evolution of dark current and photocurrent with increase in PbS doping, 35% PbS was identified as the optimal PbS doping amount. In the end, XPS measurements were done to explore the electronic structure of FAPbI<sub>3</sub>, PbS and the new hybrid material.



# **CHAPTER 1**

## **INTRODUCTION**

One of the most researched topics over the past few decades is electronics. Electronic devices have become much more efficient while their sizes have reduced from the metres range to nanometres range. Optoelectronics is the study and application of the interaction between electronic devices and light and includes devices such as solar cells, LEDs, photodiodes, et cetera. It is currently the centre of interest for many researchers working in the field of electronics and photonics.

This thesis aims at studying the optoelectronic properties of metal halide perovskites nanomaterials and developing a new compound material which uses novel properties of perovskites for infrared light detection.

### **1.1 Nanostructured Semiconductors**

The base of any electronic device is a semiconductor. Elemental semiconductors such as silicon have an indirect band gap making them poor absorbers and emitters of light. Therefore, III-V semiconductors such as GaAs and InAs with direct band gap are being used in several areas involving light. But these III-V semiconductors pose a variety of challenges including complex and expensive synthesis, difficulty in doping, and high susceptibility to impurities. This resulted in the development of II-VI and other types of semiconductors with each having their own set of challenges. To overcome these challenges, newer semiconductors are continuously being developed and researched upon.

Nanostructuring of semiconductors brings out novel physical properties such as increase in the band gap, separation of energy levels and change in density of states due to the quantum confinement effect [1]. Semiconductor nanocrystals have several benefits over bulk semiconductors. Optical properties of nanocrystals become size and shape dependent, allowing the absorption and the photoluminescence to be tuned over a broad spectral window by changing the size, shape or composition of the nanoparticle. The size of nanocrystals becomes comparable to the exciton Bohr radius of bulk material, leading to confinement of charge carriers. This promotes radiative recombination and results in increased photoluminescence.

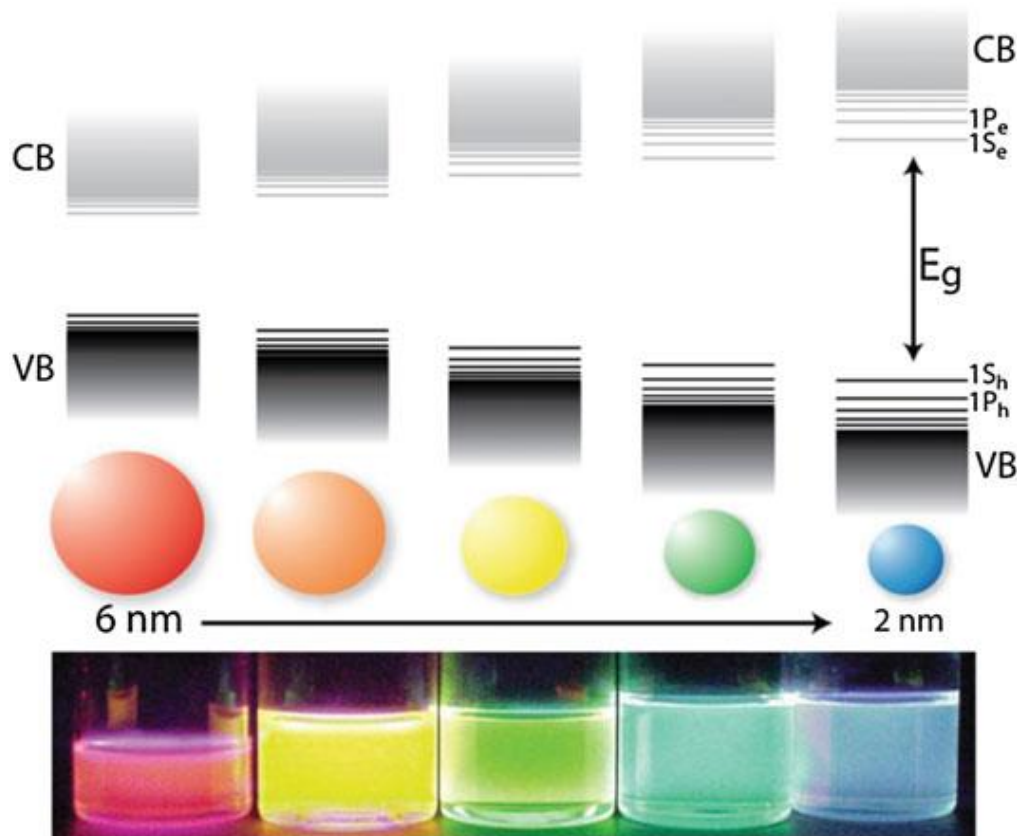


*Figure 1.1: Schematic representation of the quantum confinement effect on semiconductor nanoparticles. The colloidal suspensions of different size CdSe nanoparticles under UV light are also shown. Figure reproduced from [2].*

Semiconductors nanocrystals are commonly synthesised in two ways. Epitaxially grown semiconductor nanocrystals are grown on a substrate by methods such as vapour deposition or molecular beam epitaxy. Many III-V semiconductor nanoparticles are grown this way. Complex hetero nanostructures can be grown by this technique with precise size control [2]. Although, the complexity of this technique and requirement of specialised instruments and specific growth conditions make it time consuming, expensive and non-scalable.

Another technique for the synthesis of semiconductor nanocrystals is colloidal growth. This technique uses wet chemistry methods to grow nanoparticles in a solvent with the presence of a stabilising agent. It is relatively cheap, simple, scalable and highly versatile. Nanoparticles of different shapes, sizes, composition, and heterogeneity can be synthesised using this method by changing the composition of precursors and the environmental conditions of the synthesis.

## 1.2 Halide Perovskites

Perovskites have a general formula  $ABX_3$  where A and B are cations with A being the larger cation, while X is an anion that bonds with both A and B. In the cubic perovskite structure, the B cations form a cubic unit cell having an octahedral coordination, the A cation sits at the body centre having a 12-fold coordination, and the X anion takes the middle of the edges of the unit cell and links with 6 cations (4 A and 2 B) [3]. The structure can be slightly distorted due to certain factors.

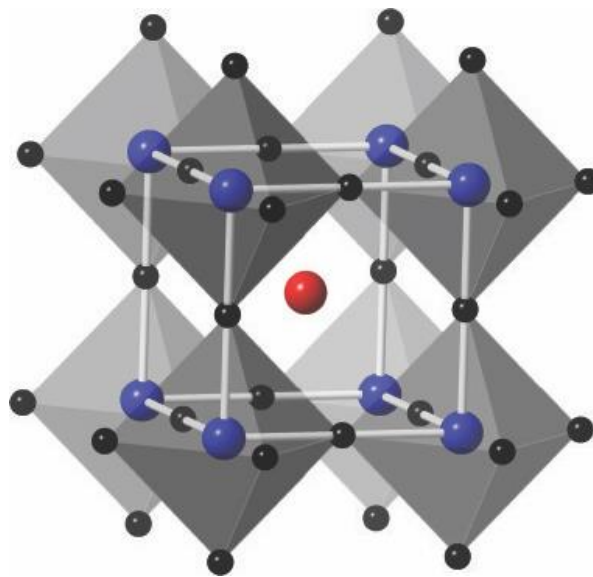


*Figure 1.2: The perovskite structure- Cubic unit cell with B cation (blue) at corners, A cation (red) at body centre and X anion (black) at edge centres. Figure reproduced from [4].*

Perovskites occur in nature as oxides of the form  $X^{II}A^{2+}VI B^{4+}O^{2-}_3$ . Synthetic perovskite oxides have also been found. Perovskite oxides show interesting properties such as ferroelectricity, ferromagnetism, dielectricity, and piezoelectricity [5].

Metal halide perovskites are the analogues of perovskite oxides of  $AMX_3$  structure where X anion is a halide and B site cation is a metal (M). Metal halide perovskites can be synthesised easily using solid as well as solution-based methods in different sizes and shapes from bulk to nanocrystals to 2D layered materials. The focus is on metal halide perovskite nanocrystals as they have an increased photoluminescence quantum yield. Nanocrystals also provide the flexibility of finely tuning the band gap by alloying multiple halide perovskites in different proportions and by introducing quantum confinement.

Metal halide perovskites are known for their defect tolerant structure. Impurities and point defects induce trap states in semiconductors. A major source of these trap states is the dangling bonds on the surface of the semiconductor. In semiconductors such as II-VI and IV-VI semiconductors, the trap states are within the band gap, which leads to energy loss to non-radiative recombination. This reduces the efficiency of optoelectronic devices made using these materials. Surface induced trap states become a huge problem in nanocrystals due to their proportionally large surface area, and passivation of the surface by growing a shell around the nanocrystal is required to minimise the trap states [6]. In metal halide perovskites, the trap states induced from typical defects are pushed into the valence and conduction bands leaving the band gap clean [7]. Due to this, electron recombination happens mostly through the radiative process, and the energy loss to heat is minimised. Metal halide perovskites nanocrystals do not require passivation of the surface and have high power conversion and photoluminescence efficiency, making them the material of choice for both solar cells and lighting applications.

### **1.3 Different Shapes and Compositions of Perovskites Nanocrystals**

Metal halide perovskite nanocrystals are most commonly synthesised as three-dimensional nanocubes (NCs) where all three dimensions are in the nanometer range but greater than the Bohr's excitonic radius. These NCs are in the weak confinement regime. Their band gap can be tuned over a range by changing the size of the NCs similar to Figure 1.1. In addition to having high power conversion efficiencies, they show photoluminescence (PL) with narrow emission line widths and high quantum yields, making them favourable for both solar cells and light emitting diodes [8]. NCs are also colloiddally stable, which results in high quality devices.

Two-dimensional metal halide perovskites nanoplatelets (NPLs) are strongly confined in one dimension and are extended in the other two, reaching up to few micrometers. The strong confinement leads to a structured absorption spectrum with sharp excitonic peaks. In addition, the confinement is quantised as the number of layers in the confined dimension. This leads to atomic level precise control in confinement in the NPLs and extremely narrow PL can be obtained compared to NCs where the PL may be broadened due to the inhomogeneity in the size of the NCs [9, 10]. The halide perovskite NPLs show higher environmental stability as the halide rich surface acts as a protective layer [11]. Perovskite NPLs can be used for specialised applications due to their large lateral extension and ability to form layered superlattices.

The optical properties of metal halide perovskites are dependent on the  $\text{MX}_6$  octahedra. Any change in the bond nature, lengths and angles of M-X bonds leads to change in the band gap of the material. It is observed that increase in the ionic nature of the M-X bond leads to increase in the band gap. Electronegativity ranges in halides as chlorine being the most electronegative followed by bromine and iodine. Hence, chloride perovskites have the widest band gap and iodide perovskites have the smallest band gaps. Similarly, lead halide perovskites have wider band gap compared to tin halide perovskites as tin is more electronegative than lead. The size and structure of A site cation indirectly affects the geometry of the  $\text{MX}_6$  octahedra, and thus, leads to some amount of change in the optoelectronic properties of the material [12]. Colloidal nanocrystals allow formation of alloys of different cations or halides by mixing of precursors or by cation/anion exchange. These mixed composition perovskites have an intermediate band gap between that of the pure perovskites, thus enabling tuning of band gap over a wide range.

#### 1.4 Motivation of this Project

Lead halide perovskites (LHPs) are the most commonly synthesised metal halide perovskites. They can be all inorganic such as Cesium Lead Halide ( $\text{CsPbX}_3$ ) or organic-inorganic such as methylammonium lead halide (MAPX) and formamidinium lead halide (FAPX). Most efficient lead halide perovskite solar cells are formed using methylammonium lead iodide (MAPI) and formamidinium lead iodide (FAPbI<sub>3</sub>). Although, FAPbI<sub>3</sub> has better optical absorption due to a smaller band gap. It also exhibits better film quality and higher phase stability within the operating conditions of a solar cell [13, 14].

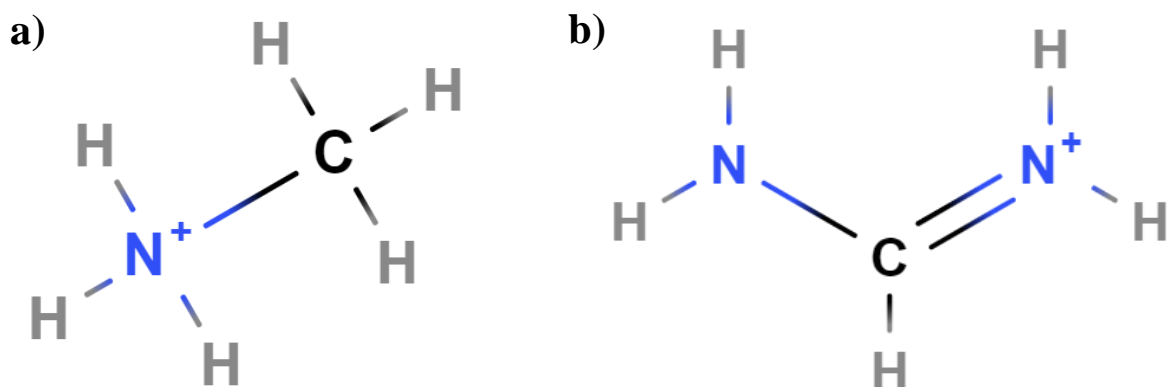


Figure 1.3: Structural formula of a) methylammonium (MA) and b) formamidinium (FA).

FAPbI<sub>3</sub> has a band gap around 1.5 eV in bulk form, absorbing and emitting in 750-800 nm range. Other LHPs have a wider band gap than FAPbI<sub>3</sub>. Thus, LHP solar cells don't absorb the near infrared (NIR) part of the solar spectrum, rendering their performance sub-optimal. Tin iodide perovskites have a smaller band gap around 1.3 eV, but their stability is significantly reduced, hence, not allowing them to be a substitute for LHPs [15]. IR absorption in halide perovskites remains a major challenge.

PbS is a IV-VI semiconductor which absorbs in the NIR region. PbS colloidal quantum dots (CQDs) are a preferred material for solar cells in the NIR range, but its power conversion efficiency is limited due to the presence of a trap state deep within the band gap. PbS devices also suffer from high dark current due to its small band gap.

By mixing FAPbI<sub>3</sub> nanocrystals and PbS CQDs, a hybrid material may be formed which absorbs in the infrared due to presence of PbS and utilise the enhanced transport properties of FAPbI<sub>3</sub>. Such a material needs to keep the properties of both FAPbI<sub>3</sub> and PbS. Also, the amount of PbS in the hybrid needs to be such that there is enough IR absorption to generate free charge carriers, and the transport is through FAPbI<sub>3</sub> which has better carrier mobility and lower dark current.

## **1.5 Work Undertaken in this Project**

I did the first part of the project at the Department of Chemistry, IISER Pune in the Optoelectronic Materials group headed by Dr. Angshuman Nag. There, I learned perovskites nanocrystal synthesis methods such as hot injection method, and characterisation methods such as Absorption Spectroscopy, Photoluminescence Spectroscopy, powder X-ray diffraction and TEM Imaging.

I performed most of the work presented in this thesis at the Institut des nanosciences de Paris (INSP), Sorbonne University in the Optoelectronics of Confined Nanomaterials (OCN) group headed by Dr. Emmanuel Lhuillier.

One of the objectives of this project was to observe and study the optoelectronic properties of perovskite nanocrystals. One of the properties observed was the dependence of the band gap on the size, shape, and composition of the nanocrystals. For this, I synthesised LHPs in different ways and recorded their absorption spectra. Different methods of synthesis, such as hot

injection method and ligand assisted precipitation were employed. LHPs of two different cations (Cs and FA) were synthesised. Mixed halide perovskites were formed by mixing precursors of different halides in various proportions. Effects of changing the temperature of synthesis and changing the composition of precursors or ligands were also observed. The changes in the band gap were observed by analysing the absorption spectra of the synthesised LHPs.

I did cleanroom fabrication of electrodes on ITO and FTO coated glass substrates and Si/SiO<sub>2</sub> wafers. I deposited films of the synthesised LHP nanocrystals on Au interdigitated electrodes and took their microscopic and profilometric images to study the film quality. I took I-V characteristics of these films using a probe setup to study the difference between dark current and photocurrent. Photosensitivity was studied by varying the intensity of illumination while photocurrent time response was studied using optical chopping of the illuminating light. I also studied the transport properties of the LHP nanocrystals at temperatures going down till 50 K.

The primary objective was to be to develop an LHP material which is able to absorb in the short-wave infrared region. To achieve this, FAPI nanocrystals and PbS CQDs were synthesised and were mixed in different proportions to form a hybrid material. Structural and optoelectronic properties of these mixtures were studied to confirm the formation of the hybrid material and to determine the right proportion of FAPI:PbS such that the hybrid material shows the desired properties. I learned X-ray photoemission spectroscopy at the TEMPO beamline of the SOLEIL Synchrotron facility as part of this project. This part of the project was done in collaboration with Prachi Rastogi, a post-doctoral student in the OCN group.

I worked on another project related to HgTe nanoplatelets which is not included in this thesis. I performed pressure-resolved X-ray diffraction on HgTe nanoplatelets. A diamond anvil cell (DAC) was used to introduce pressure in the GPa range, and the pressure was determined using photoluminescence from ruby spheres that were added to the DAC. I also performed pressure and temperature resolved IR spectroscopy at the SMIS beamline of the SOLEIL Synchrotron facility. Liquid helium induced cryocooling was used to introduce temperature resolution. This project was done in collaboration with two PhD students, Charlie Gréboval from the OCN group and Nicolas Moghaddam from a collaborating group.



## **CHAPTER 2**

### **MATERIALS AND METHODS**

In this thesis, most of the LHP nanoparticles were synthesised using the colloidal growth method known as hot injection method. In this method, lead halide precursors were mixed in a solvent such as octadecene along with ligands and stabilising agents such as oleic acid and oleylamine, and kept in an inert atmosphere. Oleate precursors of the A site cation were injected at the desired temperature to form the nanoparticles which were insoluble in the solvent used. Centrifugation was used to isolate the nanoparticles which were then suspended in nonpolar solvents such as toluene or hexane. The nanoparticles were washed with low polar solvent such as ethyl acetate to remove excess ligands. Other synthesis methods used included ligand assisted reprecipitation where the precursors were added at the same time to the solvent already containing the ligands and LHP nanocrystals were formed spontaneously. Cation exchange was also used. The synthesised LHPs were then characterised using absorption spectroscopy, photoluminescence spectroscopy, X-ray diffraction, TEM imaging, and X-ray photoemission spectroscopy. Interdigitated electrodes were fabricated and nanocrystals films were deposited on them. These were then characterised for transport properties.

Step-by-step procedures for the synthesis and the characterisation in detail are given below.

#### **PART A: Experiments done at IISER Pune**

### **2.1 Synthesis Methods for FAPI**

#### **2.1.1 List of Chemicals Used**

Formamidinium Acetate (FA Acetate) (99%), Lead Iodide ( $\text{PbI}_2$ ) (99.999%, trace metals basis), Cesium Iodide (CsI) (99.9%, trace metals basis), Formamidinium Iodide (FAI) ( $\geq 99\%$ , anhydrous), Octadecene (ODE) (90%, technical grade), Oleylamine (OLA) (70%, technical grade), Oleic Acid (OA) (90%, technical grade), Octadecylamine ( $\geq 99.0\%$ ), Dodecylamine (98%), Octylamine (99%), Toluene ( $\geq 99.5\%$ , ACS reagent), Toluene (99.8%, anhydrous), Dimethyl Sulfoxide (DMSO) ( $\geq 99.9\%$ , anhydrous), and N,N-Dimethylformamide (DMF)

(99.8%, anhydrous) from Sigma-Aldrich; Hexane (ACS reagent), Ethyl Acetate (AR), Acetic Acid (glacial, AR), Hydroiodic Acid (HI) (57 wt%, LR), and Diethyl Ether (LR) from Rankem.

### 2.1.2 Formamidinium Oleate Synthesis (From [16])

521 mg FA acetate (5.0 mmol), 16 mL ODE, and 4 mL OA are taken in a round bottom flask and heated to 100 °C under an N<sub>2</sub> atmosphere. It is degassed under vacuum for 30 minutes. The atmosphere in the flask is switched back to N<sub>2</sub>, and it is heated to 130 °C. It is then stirred till a clear yellow solution is obtained. It is then cooled down to 80 °C and degassed for 10 minutes. This solution is stored in an N<sub>2</sub> purged vial and is heated to 100 °C before use.

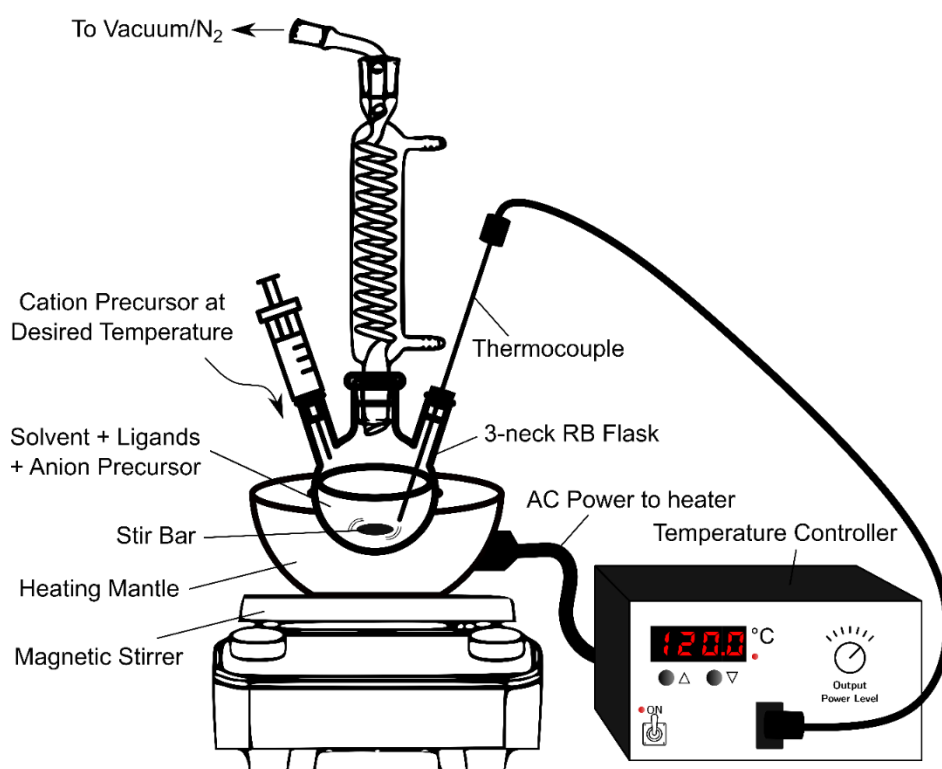


*Figure 2.1: Scheme of hot injection method used for synthesis.*

### 2.1.3 Formamidinium Lead Iodide (FAPI) Nanocubes (NCs) Synthesis (From [16])

173 mg PbI<sub>2</sub> (0.375 mmol), 10 mL ODE, 2 mL OA, and 1 mL OLA are taken in a round bottom flask and heated to 120 °C under an N<sub>2</sub> atmosphere. It is stirred till a clear solution is obtained. It is then degassed under vacuum for 30 minutes. The atmosphere in the flask is switched back to N<sub>2</sub>, and the solution is cooled down to 80 °C. 4 mL of the prepared Formamidinium Oleate

solution is quickly injected. The solution turns dark red immediately. After 5 s, the solution is cooled to room temperature using a water bath. It is then centrifuged at 7800 rpm. The supernatant is discarded, and the precipitate is redispersed in toluene. Ethyl acetate is added to the solution to precipitate the nanocrystals, and it is centrifuged again. The supernatant is discarded, and the precipitate is redispersed in toluene. Ethyl acetate washing step is repeated 2 more times, and the final precipitate is redispersed in anhydrous toluene.

#### 2.1.4 Formamidinium Lead Iodide (FAPI) Nanoplatelets (NPLs) Synthesis using Hot Injection Method

The solution is cooled down to 40 °C before Formamidinium Oleate injection. Rest of the procedure is the same as 2.1.3.

#### 2.1.5 Formamidinium Lead Iodide (FAPI) NPLs Synthesis using Cation Exchange Method (Modified from [17])

Inside the glove box- 230 mg  $\text{PbI}_2$  (0.5 mmol), 260 mg CsI (1.0 mmol), and 7.5 mL DMSO are taken in a glass vial and mixed to form a clear solution. It is named 'A'. 0.5 g octadecylamine and 2.5 mL acetic acid are taken in a glass vial and mixed to form a clear solution. It is named 'B'. 104 mg FA acetate and 2 mL acetic acid are taken in a glass vial and mixed to form a clear solution. It is named 'C'. 0.6 g dodecylamine and 3 mL acetic acid are taken in a glass vial and mixed to form a clear solution. It is named 'D'.

1.5 mL of 'B' is taken in a glass vial and put on stirring. 0.23 mL of 'A' is added to it. A yellow turbid solution is obtained. It is sonicated for 10 minutes. Acetic acid is added to it, and it is centrifuged to obtain a yellow precipitate. This centrifugation is repeated twice, and the final precipitate is redispersed in 10 mL anhydrous toluene. This material is Octadecylammonium Lead Iodide (OAPI).

The above solution is taken in a glass vial and put on stirring. 0.2 mL of 'D' is added to it. Approximately 60  $\mu\text{L}$  of 'C' is swiftly added to it. The solution turned brown. It is stirred for 10 minutes and then centrifuged to obtain a brown precipitate. Anhydrous toluene is added to it, and it is centrifuged again. The supernatant is discarded, and the precipitate is redispersed in anhydrous toluene.

### 2.1.6 Formamidinium Lead Iodide (FAPI) NPLs Synthesis by Ligand Assisted Reprecipitation (LARP) Method (From [4])

A beaker is placed in an ice-water bath. 10 mL of octylamine is added to it and put on stirring. 10 mL HI added to it dropwise. It is left on stirring for at least 2 hours. It is then kept on 90 °C overnight inside the fume hood to evaporate water. It is washed with diethyl ether using filter paper twice and then put in vacuum at 75 °C overnight to dry completely. The yellow powder obtained is then transferred to the glove box. It is Octylammonium Iodide (OctAmI).

52 mg OctAmI (0.2 mmol) and 2 mL DMF are taken in a glass vial and mixed to form a clear solution. It is named 'L'. 35 mg FAI (0.2 mmol) and 2 mL DMF are taken in a glass vial and mixed to form a clear solution. It is named 'A'. 93 mg FAI (0.2 mmol) and 2 mL DMF are taken in a glass vial and mixed. It is sonicated and passed through a PTFE filter to form a clear solution. It is named 'B'. 100  $\mu$ L 'B', 50  $\mu$ L 'A' and 400  $\mu$ L 'L' are mixed in a glass vial to make the precursor solution.

5 mL anhydrous toluene is taken in a glass vial and put on stirring. 50  $\mu$ L precursor solution is swiftly added to it. The solution turned red. It is centrifuged at 7800 rpm. The supernatant is discarded, and the precipitate is redispersed in anhydrous toluene.

## **2.2 Characterisation of Materials**

### 2.2.1 UV-Vis Absorption Spectroscopy

The FAPI solution is diluted in toluene, and the absorption spectrum is acquired using a Cary 300 UV-Vis spectrophotometer.

### 2.2.2 Photoluminescence Spectroscopy

The FAPI solution is diluted in toluene, and the photoluminescence spectrum is obtained using an Edinburg FLS 980 spectrophotometer. Photoluminescence decay is measured using an EPL-405 picosecond pulsed 405 nm diode laser while operating the instrument in the time-correlated single-photon counting (TCSPC) mode.

### 2.2.3 Transmission Electron Microscopy (TEM)

The FAPI solution is diluted, and a small amount is dropped on a copper grid. The grid is degassed overnight under secondary vacuum, and TEM images are acquired using a JEOL JEM-2200FS.

### 2.2.4 Powder X-Ray Diffraction (pXRD)

A glass slide is wiped cleaned using acetone. 50-100  $\mu\text{L}$  of the FAPI solution is dropped on the glass slide, and let it stay in the air to allow the solvent to dry. The pXRD measurement is done on this slide using Bruker D8 Advance x-ray diffractometer with Cu  $K\alpha$  radiation (1.54  $\text{\AA}$ ).

## **PART B: Experiments done at INSP, Sorbonne University**

### **2.3 Synthesis Methods for Perovskites and Other Materials**

#### 2.3.1 List of Chemicals Used

Formamidinium Acetate (FA Acetate) (99%), Lead Bromide ( $\text{PbBr}_2$ ) (98+%), Lead Iodide ( $\text{PbI}_2$ ) (98.5%), Cesium Carbonate ( $\text{Cs}_2\text{CO}_3$ ) (99%, metals basis), Sulphur (S) powder (sublimed, 100 mesh, 99.5%), Octadecene (ODE) (90%, technical grade), and Oleic Acid (OA) (90%, technical grade) from Alfa Aesar; Oleylamine (OLA) (80-90%), n-Octylamine (OctAm) (99+%), Octanoic Acid (OctAc) (99%), and Hydrobromic Acid (HBr) (48 wt%) from Arcos Organics; Toluene ( $\geq 99\%$ , GPR grade), Hexane ( $\geq 95\%$ , technical grade), Acetone ( $\geq 99\%$ , technical grade), and N,N-Dimethylformamide (DMF) ( $\geq 99.5\%$ , GPR grade) from VWR Chemicals; Ethyl Acetate ( $\geq 99.8\%$ ) from JT Baker.

#### 2.3.2 Formamidinium Oleate Synthesis (From [18])

390 mg FA acetate (3.75 mmol), 18 mL ODE, and 12 mL OA are taken in a round bottom flask and degassed at room temperature for 45 minutes. The mixture is then heated to 100  $^\circ\text{C}$  under vacuum and stirred till a clear yellow solution is obtained. This solution is heated to 100  $^\circ\text{C}$  before use.

### 2.3.3 Formamidinium Lead Iodide (FAPbI<sub>3</sub>) NCs Synthesis (From [18])

240 mg PbI<sub>2</sub> (0.52 mmol) and 18 mL ODE are taken in a round bottom flask and degassed at room temperature for 15 minutes. The solution is then heated to 110 °C under vacuum. 4 mL OA and 2 mL OLA are injected, and the solution is degassed for 15 minutes. Lead salt dissolves completely, and a clear solution is obtained. The atmosphere in the flask is switched to N<sub>2</sub>, and the solution is cooled down to 80 °C. 20 mL of the prepared Formamidinium Oleate solution is quickly injected. The solution turns dark red immediately. After 15 s, the solution is cooled to room temperature using a water bath. It is then centrifuged at 6000 rpm. The supernatant is discarded, and the precipitate is redispersed in hexane. Ethyl acetate is added to the solution to precipitate the nanocrystals, and it is centrifuged again. The supernatant is discarded, and the precipitate is redispersed in toluene. The solution is centrifuged again at slow speed to remove the unstable phase.

### 2.3.4 Formamidinium Lead Bromide-Iodide (FAPbBrI) Synthesis

PbBr<sub>2</sub> and PbI<sub>2</sub> are taken in desired proportion keeping the net PbX<sub>2</sub> amount to 0.52 mmol (191 mg PbBr<sub>2</sub> for FAPbBr). The solution is heated/cooled down to the desired temperature before Formamidinium Oleate injection. Rest of the procedure is the same as 2.3.3.

### 2.3.5 Lead Sulphide (PbS) CQDs Synthesis (From [19])

38 mg Sulphur powder (1.2 mmol) and 7.5 mL OLA are taken in a glass vial and sonicated till the complete dissolution of S powder. 370 mg PbCl<sub>2</sub> (1.33 mmol) and 7.5 mL OLA are taken in a round bottom flask and degassed at room temperature for 40 minutes. The solution is then heated to 110 °C under vacuum and degassed for 30 minutes. The atmosphere in the flask is switched to N<sub>2</sub>, and the solution is heated to 140 °C. The S-OLA solution is injected into the flask at 140 °C. A mixture of 1 mL OA and 10 mL Hexane is prepared and injected into the flask after 18 minutes to quench the reaction. The solution is cooled down to room temperature using a water bath, and ethanol is added to it to initiate precipitation. It is then centrifuged at 4500 rpm for 5 minutes. The supernatant is discarded, and the precipitate is redispersed in toluene. Ethanol is added, and it is centrifuged again. The supernatant is discarded, and the precipitate is dried in a vacuum chamber for 30 minutes. It is redispersed in toluene and

centrifuged to remove the unstable phase. The supernatant is filtered using a 0.2  $\mu\text{m}$  PTFE filter.

### 2.3.6 Preparation of FAPI-PbS Hybrid

The FAPI NCs solution in toluene and the PbS CQDs solution in toluene are taken in known concentration and then mixed together in the desired proportion. The solution is then mixed well using vortex or sonication.

### 2.3.7 Cesium Oleate Synthesis (From [20])

350 mg  $\text{Cs}_2\text{CO}_3$  (1.07 mmol), 20 mL ODE, and 1.25 mL OA are taken in a round bottom flask and degassed at room temperature for 30 minutes. The solution is then heated to 110  $^\circ\text{C}$  under vacuum and degassed for 30 minutes. The atmosphere in the flask is switched to  $\text{N}_2$ , and the solution is heated to 150  $^\circ\text{C}$ . The solution is stirred till Cs salt is fully dissolved (indicated by yellow colour). It is cooled down to 80  $^\circ\text{C}$  and degassed for 5 minutes. This solution is heated to 100  $^\circ\text{C}$  before use.

### 2.3.8 Cesium Lead Halide ( $\text{CsPbX}_3$ ) NCs Synthesis (From [21])

0.4 mmol  $\text{PbX}_2$  (147 mg  $\text{PbBr}_2$ , 185 mg  $\text{PbI}_2$ , or desired proportion of both) and 10 mL ODE are taken in a round bottom flask and degassed at room temperature for 15 minutes. The solution is then heated to 110  $^\circ\text{C}$  under vacuum. 0.5 mL OA and 0.5 mL OLA are injected, and the solution is degassed for 15 minutes. Lead salt dissolves completely, and a clear solution is obtained. The atmosphere in the flask is switched to  $\text{N}_2$ , and the solution is heated to 180  $^\circ\text{C}$ . 1 mL of the prepared Cesium Oleate solution is quickly injected. The solution changes colour immediately. After 30 s, the solution is rapidly cooled to room temperature using an ice water bath. It is then centrifuged at 6000 rpm. The supernatant is discarded, and the precipitate is redispersed in hexane. Ethyl acetate is added to the solution to precipitate the nanocrystals, and it is centrifuged again. The supernatant is discarded, and the precipitate is redispersed in toluene. The solution is centrifuged again to remove the unstable phase.

### 2.3.9 Cesium Lead Bromide (CsPbBr<sub>3</sub>) NPLs Room Temperature Synthesis (From [20])

735 mg PbBr<sub>2</sub> (2.0 mmol) and 5 mL DMF are taken in a glass vial and sonicated till PbBr<sub>2</sub> is completely dissolved. 10 mL ODE, 1 mL OA, and 1 mL OLA are taken in a 100 mL beaker and put on stirring. 0.8 mL of the prepared Cesium Oleate solution is added to it. The PbBr<sub>2</sub>-DMF solution is swiftly added to it, and after 10 s, 40 mL acetone is swiftly added to quench the reaction. The solution is stirred till a colour change to green is observed. It is then centrifuged at 6000 rpm. The supernatant is discarded, and the precipitate is redispersed in hexane. It is centrifuged again, and the supernatant (stable phase) is separated and stored. The precipitate (unstable phase) is redispersed in hexane and stored.

Modifications to this procedure include the addition of 240 µL HBr in the beaker before the introduction of PbBr<sub>2</sub>-DMF solution and use of OctAc instead of OA / use of OctAm instead of OLA.

### 2.3.10 CsPbBr<sub>3</sub> Ligand-Assisted Nanosheets (NSs) Synthesis (From [22])

170 mg PbBr<sub>2</sub> (0.47 mmol) and 10 mL ODE are taken in a round bottom flask and degassed at room temperature for 15 minutes. The solution is then heated to 110 °C under vacuum. 1.1 mL OA, 0.25 mL OLA, 0.75 mL OctAc, and 0.75 mL OctAm are injected, and the solution is degassed for 15 minutes. Lead salt dissolves completely, and a clear solution is obtained. The atmosphere in the flask is switched to N<sub>2</sub>, and the solution is heated to 150 °C. 0.1 mL of the prepared Cesium Oleate solution is quickly injected. The solution changes colour immediately. It is kept stirring at 150 °C for 35 minutes and then is rapidly cooled to room temperature using an ice water bath. It is then centrifuged at 6000 rpm. The supernatant is discarded, and the precipitate is redispersed in toluene. It is centrifuged again, and the supernatant (stable phase) is separated and stored. The precipitate (unstable phase) is redispersed in toluene and stored.

## 2.4 **Device Fabrication**

### 2.4.1 Fabrication of Au Interdigitated Electrodes on Si/SiO<sub>2</sub> Wafers

The surface of an Si/SiO<sub>2</sub> wafer (400 nm thick SiO<sub>2</sub> layer) is cleaned by sonication in acetone, rinsing with isopropanol and cleaning with O<sub>2</sub> plasma. Microchemicals AZ 5214 E photoresist

is spin-coated on the wafer and baked at 110 °C for 90 s. It is then exposed to UV through a patterned mask for 2 s using SUSS Microtec MJB4. The wafer is further baked at 125 °C for 2 minutes to invert the resist. A 40 s UV flood exposure is performed on the wafer. It is then developed by dipping in a bath of Microchemicals AZ 726 MIF developer for 32 s, followed by rinsing in pure water. A 3 nm chromium layer and a 40 nm gold layer are deposited on the wafer using a Vinci PVD4 thermal evaporation deposition (TVD) system. It is then dipped in acetone for 1 hour for resist lift-off, after which it is rinsed with isopropanol and dried off. The electrodes are 2.5 mm long and 10 μm wide with a spacing of 10 μm between them.

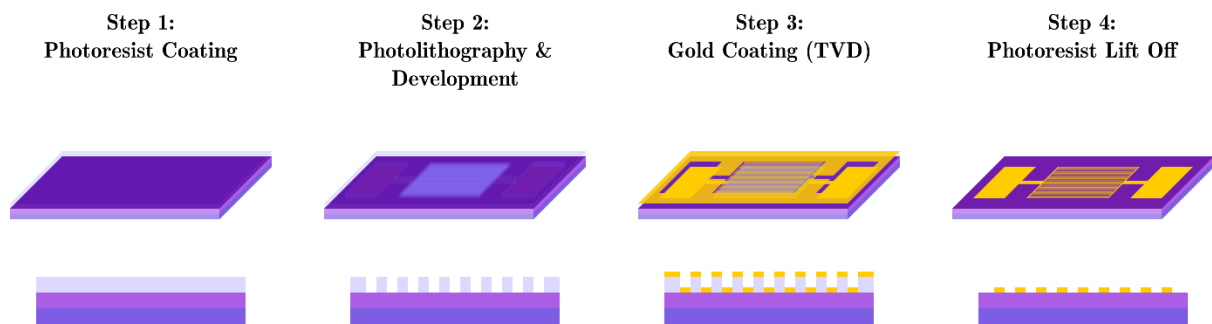


*Figure 2.2: Scheme of fabrication of Au interdigitated electrodes on Si/SiO<sub>2</sub> wafers.*

#### 2.4.2 Film Preparation by Dropcasting

The substrate (Si/SiO<sub>2</sub> wafer) is rinsed in acetone and isopropanol and dried off with an N<sub>2</sub> gun. 5-10 μL of the perovskites solution is dropped on the substrate, ensuring coverage of the whole active area. It is then kept in the air to allow the solvent to evaporate.

#### 2.4.3 Film Preparation by Spin-coating

The substrate is rinsed in acetone and isopropanol and dried with an N<sub>2</sub> gun. It is kept on spin-coater, and 5-10 μL of the perovskites solution is dropped on it, ensuring coverage of the whole area. It is then spin-coated at 1500-2000 rpm for 20-30 s.

#### 2.4.4 Ligand Exchange on the Film

A ligand exchange solution is prepared by making a saturated solution of lead acetate in ethyl acetate and removing excess undissolved lead acetate by centrifugation. The dropcasted or

spin-coated film is dipped in the lead acetate in ethyl acetate solution for 30 s followed by dipping in neat ethyl acetate for 30 s and then dried with an N<sub>2</sub> gun. Multiple layers of films are prepared by repeating the dropcasting/spin-coating step and ligand exchange step subsequently multiple times until the desired thickness is achieved.

## **2.5 Characterisation of Materials**

### **2.5.1 UV-Vis Absorption Spectroscopy**

The perovskites solution is diluted in hexane, and the absorption spectrum is acquired using a JASCO V-730 spectrophotometer.

### **2.5.2 NIR Absorption Spectroscopy**

A Thermo Scientific Nicolet iS50 FTIR spectrometer is used in ATR configuration to acquire an NIR absorption spectrum for the PbS solution. For this, a drop of PbS solution is put on the diamond window and dried. The in-built white light source is used with a CaF<sub>2</sub> beamsplitter and a DTGS ATR detector. The output is averaged over 32 spectra.

### **2.5.3 Transmission Electron Microscopy (TEM)**

The nanocrystals solution is diluted, and a small amount is dropped on a copper grid. The grid is degassed overnight under secondary vacuum, and TEM images are acquired using either a JEOL JEM-2010 microscope or an FEI Titan Themis 200 microscope.

### **2.5.4 X-Ray Photoemission Spectroscopy (XPS)**

XPS measurements are performed at the TEMPO beamline XPS setup at the SOLEIL Synchrotron facility. 5 nm Cr layer and 80 nm Au layer is deposited on a clean Si wafer using TVD. Film of synthesised material is deposited in the same way as it is deposited on interdigitated electrode devices. Ligand exchange, if required, is also performed in the same way. The sample is introduced in the preparation chamber of the XPS setup and is degassed till a vacuum below 10<sup>-9</sup> millibar is reached. It is then moved to the analysis chamber where it is irradiated with a photon beam of energy 600 eV (for binding energy measurements) or 100 eV (for valence band and work function measurements). The emitted electron signal is acquired on an MBS A-1 photoelectron analyser equipped with an Elettra delay line detector. The pass

energy is kept fixed at 50 eV for all measurements. The photon energy value is calibrated by fixing the Au fermi energy to zero or by fixing the position of Au 4f core level peaks to a fixed energy.

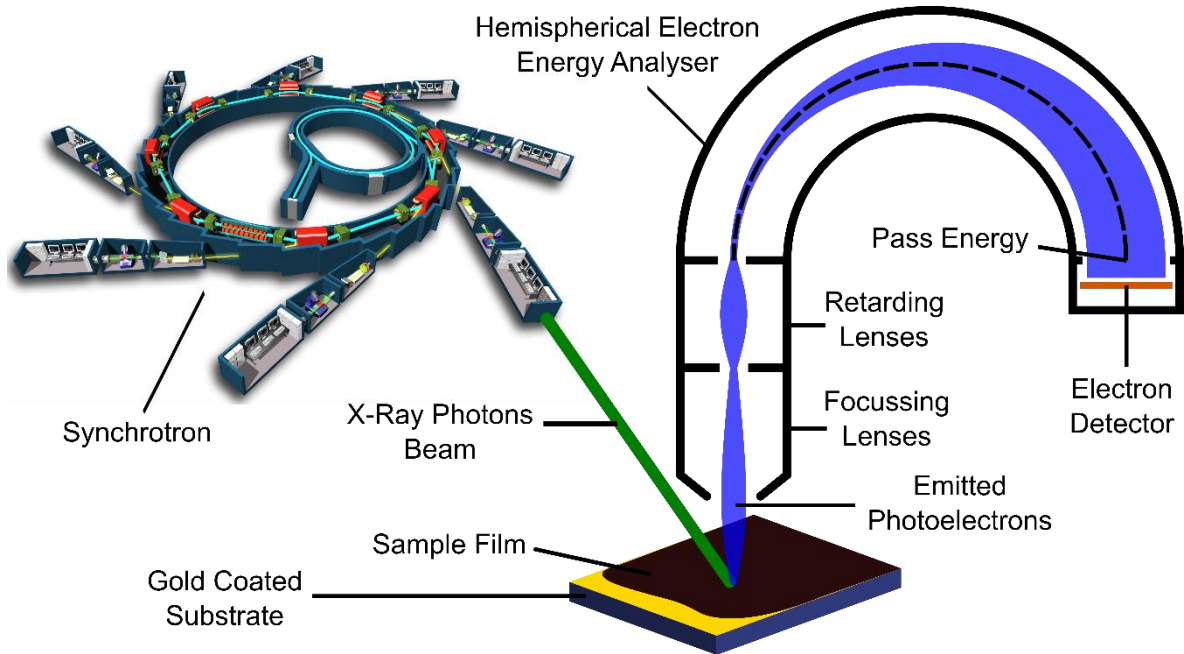


Figure 2.3: Scheme of X-ray photoemission spectroscopy.

## 2.6 Characterisation of Devices

### 2.6.1 Probe Setup for Transport Measurements

The electrode pads are cleaned of the film using a cotton swab. The substrate is then placed at a probe station, and the probe tips are connected to the contact pads. The tips are connected to a Keithley 2634B SourceMeter which is used to provide a voltage bias between the probes and also to measure the current between them. The SourceMeter is driven using a LabVIEW program.

A Coherent CUBE 405-50C 405 nm laser diode is aligned on the electrodes using a mirror. The power of the incident light on the sample is tuned by either changing the current to the diode or adding an optical density filter ( $OD = 2$ ) on the optical path to the sample, or by a combination of both. Current vs voltage (I-V) measurements are done under dark conditions (unilluminated sample) and under the illumination of the laser at different powers.

For FAPI-PbS, absorption of short-wave infrared by the sample is observed. Hence, a 1.55  $\mu\text{m}$  laser diode is used instead of the 405 nm laser. It is driven by a power supply. The power of the laser is varied by changing the current to the diode.

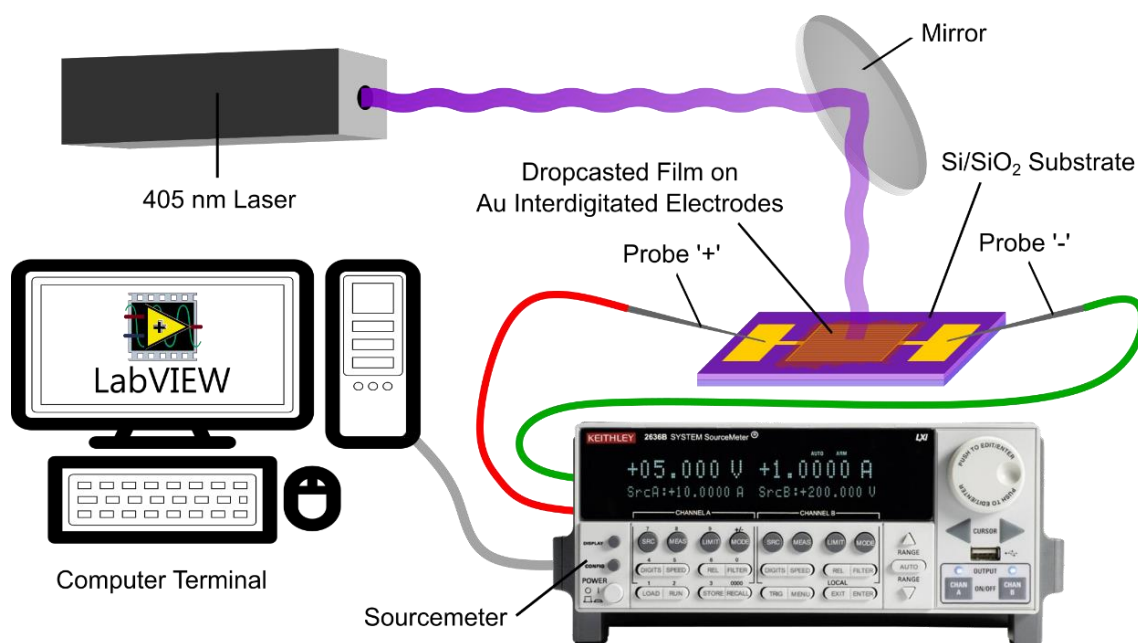


Figure 2.4: Scheme of the probe setup.

## 2.6.2 Low Temperature Setup for Transport Measurements

Two copper contacts are attached to the cold finger of an APD DE-202A closed circuit helium cryocooler and are connected to a Keithley 2634B SourceMeter through the cryocooler head. The SourceMeter is attached to a computer loaded with the same LabVIEW program mentioned above. The substrate's pads are attached to the copper contacts using silver paint. A heater is attached to the cold finger, and temperature sensors are attached to the cold finger and to a copper contact. The heater and the sensors are connected to a LakeShore 325 temperature controller which is used to regulate the temperature of the sample.

The sample is put under vacuum to avoid thermal loss. The 405 nm laser is aligned on the sample through the cryocooler chamber window. I-V measurements are performed as in 2.6.1 at room temperature and at lower temperatures. Additionally, the current is measured as a function of temperature as the sample is cooled down.

### 2.6.3 Setup for Photocurrent Spectrum Measurements

The electrode pads of the substrate are connected to the input of a FEMTO DLPCA-200 current amplifier. The voltage bias is applied using the amplifier. The substrate is kept at the external detector window of a Thermo Scientific Nicolet iS50 FTIR spectrometer. The spectrometer is first calibrated using the in-built white light source and the DTGS detector with an empty sample compartment. It is then operated in external detector mode using the same source and an empty sample compartment. The output signal from the amplifier is fed to the instrument's acquisition board.

## 2.7 **Data Analysis**

All the processing of data and the plotting of graphs is done using the OriginPro software.



# CHAPTER 3

## RESULTS AND DISCUSSION

### 3.1 Characterisation of FAPI Nanocrystals Synthesised at IISER Pune

I first synthesised FAPI NCs during the first part of the project at IISER Pune, as mentioned in 2.1.3. I characterised the synthesised NCs using different methods as summarised below.

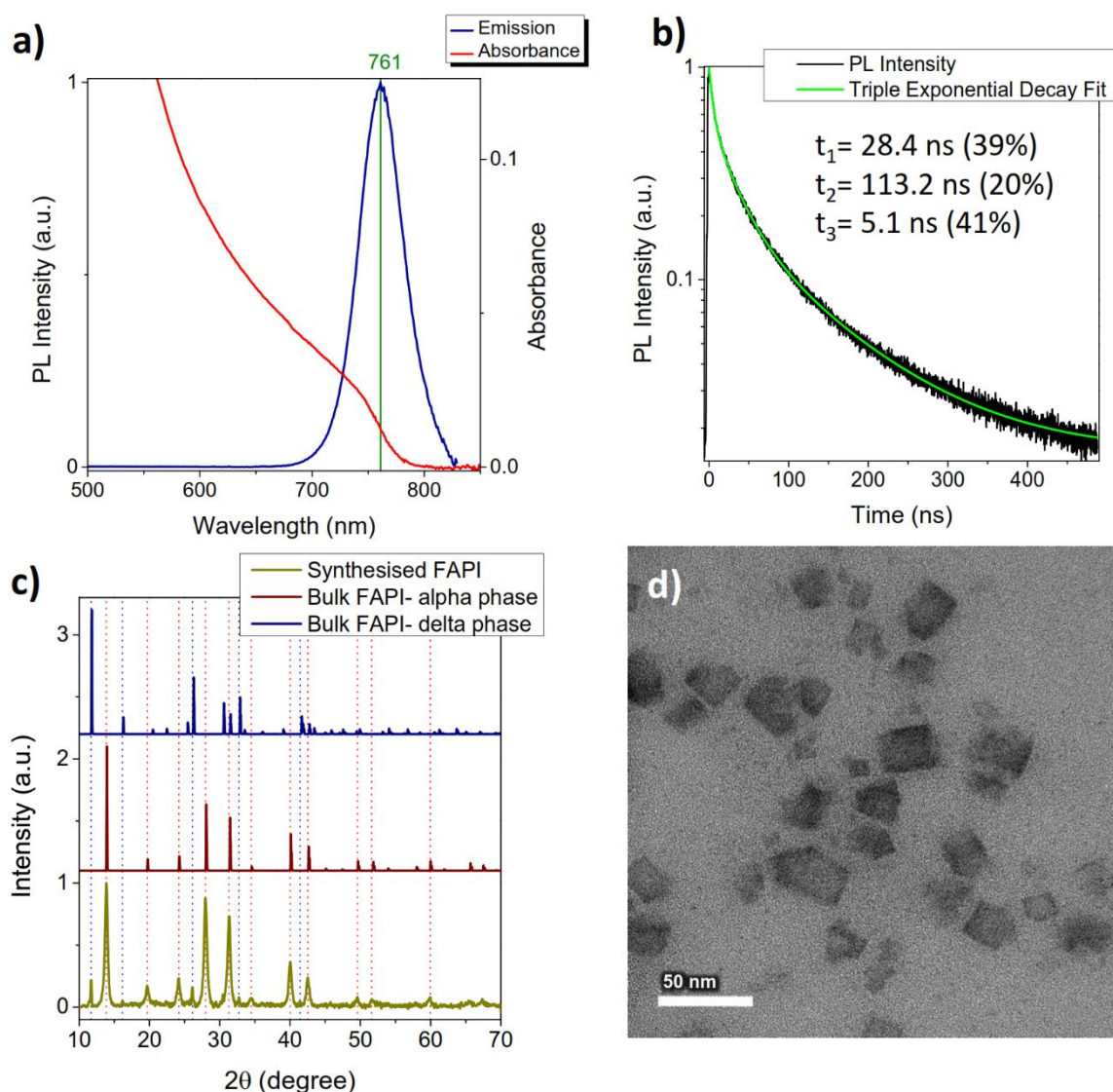


Figure 3.1: a) UV-Vis absorption and photoluminescence emission spectrum, b) Photoluminescence decay spectrum using 405 nm laser showing average lifetime of 36 ns, c) pXRD pattern compared to CIF data of  $\alpha$  and  $\delta$ -phases of bulk FAPI, and d) TEM image of synthesised FAPI nanocrystals (Scale = 50 nm).

The absorption spectrum showed a peak at 750 nm wavelength, which signifies the energy gap between the first available transition bands for excitation of electrons from the valence band to the conduction band. This value is always greater than (in energy terms) but close to the band gap of the material. In a clean band gap material like FAPI, the recombination of charge carriers occurs between the minima of conduction bands (LUMO) and the maxima of valence bands (HOMO). Therefore, the photoluminescence maxima, which was at 761 nm in this case, occurs at the wavelength corresponding to the band gap. This implies that the band gap of this batch of FAPI NCs is 1.63 eV and is close to the absorption peak. Thus, one can estimate the band gap of a nanomaterial from the wavelength of the absorption peak.

I used TCSPC for measuring the photoluminescence decay at 405 nm excitation wavelength. I fitted the spectrum with a triexponential decay fit and found the average photoluminescence lifetime to be 36 ns. A long recombination lifetime is desired in solar cells as it allows the generated charge carriers to drift away before recombining and becoming unavailable.

The powder X-ray diffractogram of the synthesised FAPI NCs was matched with the CIF data for the  $\alpha$  and  $\delta$ -phases of bulk FAPI.  $\alpha$ -phase is the cubic perovskite phase of FAPI with a 1.5 eV band gap (for bulk).  $\delta$ -phase of FAPI is the yellow hexagonal phase with a much wider band gap (around 2.3 eV) [23].  $\delta$ -FAPI could have formed due to excessive post-synthesis cleaning of FAPI NCs. The CIF data was taken from [24].

The TEM image showed that the FAPI nanocrystals were indeed in nanocubes form with some degree of inhomogeneity in the shape. The NCs were approximately 20 nm in size. This is greater than the exciton Bohr radius for FAPI. The NCs are in weak confinement regime as one can observe an increase in the band gap compared to the bulk. The absence of a separated absorption peak suggests that there is no band separation which also means that strong confinement is absent.

The presence of  $\delta$ -phase and inhomogeneous shape of NCs suggested that the FAPI nanoparticles formed had unwanted components.

I made efforts to synthesise FAPI NPLs using three different methods, but all of them failed to give the desired product. A product was formed in each case, but the absorption, photoluminescence and pXRD spectra were different from what was expected.

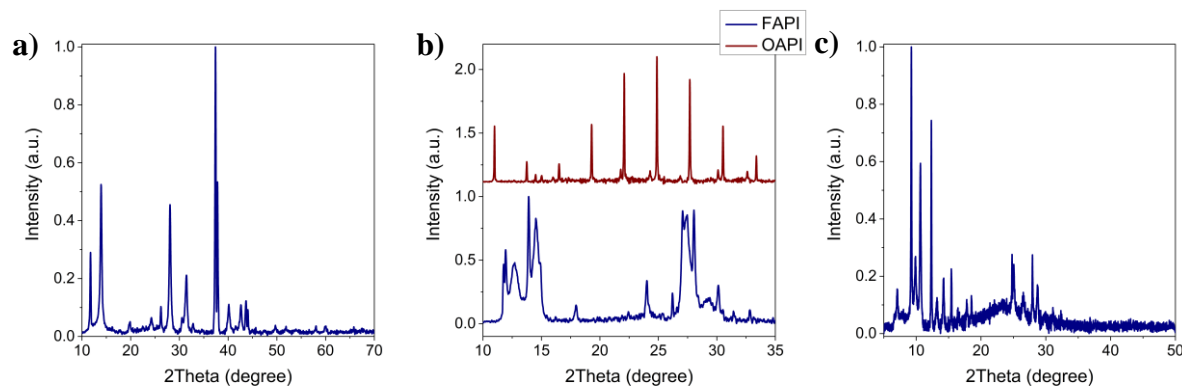


Figure 3.2: pXRD of 'not' FAPI NPLs obtained by a) hot injection method (2.1.4), b) cation exchange method (2.1.5), and c) LARP method (2.1.6).

The material obtained in the first case showed the characteristic peaks of FAPI but width of pXRD peaks and the position of absorption/photoluminescence peaks indicated that NPLs had not been formed. In the other two cases, there was no evidence of FAPI characteristics. Although, the intermediate OAPI in second case showed evidence of a layered structure as was expected.

## 3.2 Band Gap Tuning Through Size, Shape and Composition of Nanocrystals

The size, shape and composition of LHP nanocrystals were modified by a variety of methods as given below.

### 3.2.1 Change in Confinement through Temperature of Synthesis

In hot injection method, the perovskite nanocrystals start forming immediately after the second set of precursors is injected. Hence, the temperature of injection is the temperature of synthesis. This temperature plays a crucial role in determining the shape and size of the nanocrystals formed. NCs are formed at a particular temperature which is specific to the composition of the LHP. Below this temperature, NPLs start growing along with NCs. If the temperature is reduced further, NCs can't be formed, and only NPLs are obtained. NPLs are strongly confined

in only one direction. This heterogeneity of confinement leads to band separation and widening of the band gap.

Here, I synthesised  $\text{CsPbBr}_3$  and  $\text{FAPbBr}_3$  by hot injection method (2.3.8 and 2.3.4 respectively) while varying the temperature at which the Oleate precursor was injected.

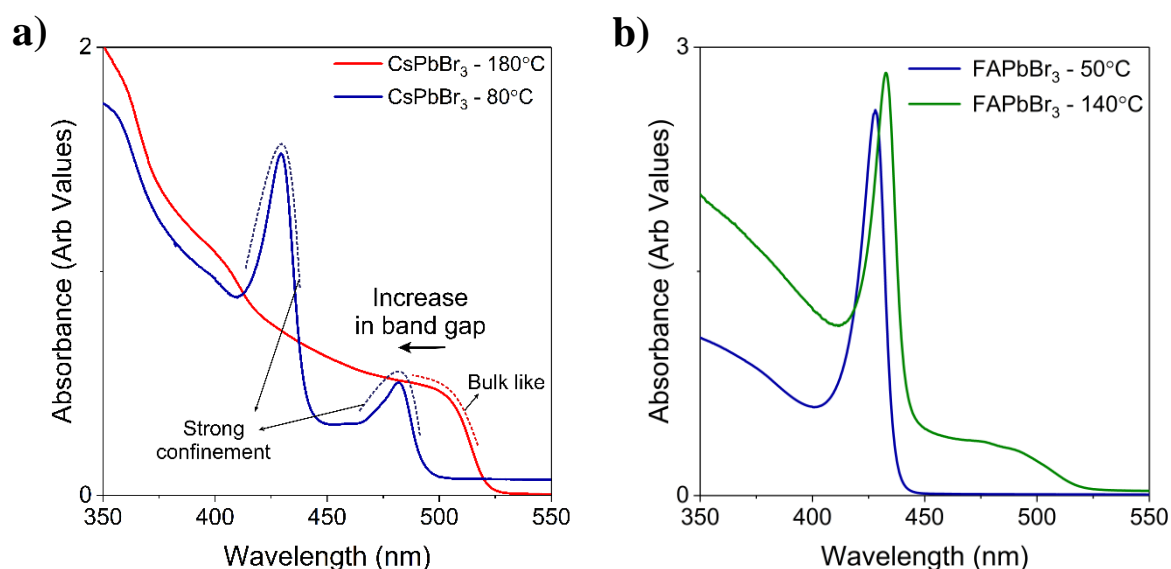


*Figure 3.3: Absorption spectra for a)  $\text{CsPbBr}_3$  and b)  $\text{FAPbBr}_3$  synthesised by hot injection method at varying temperature of precursor injection.*

When I injected the precursor at 180 °C,  $\text{CsPbBr}_3$  NCs with bulk-like absorption at 500 nm were obtained. But when the precursor was injected at 80 °C, two species of  $\text{CsPbBr}_3$  NPLs with thick NPLs having absorption at 482 nm and much thinner NPLs having absorption at 429.6 nm were obtained [25]. The thin NPLs seemed to be only a few layers thick.

In the case of  $\text{FAPbBr}_3$ , NCs with absorption at 492 nm and NPLs with absorption at 432.8 nm were obtained when I injected the precursor at 140 °C. This signifies that the optimum temperature for formation of  $\text{FAPbBr}_3$  NCs synthesis is greater than 140 °C. When the precursor was injected at 50 °C, only NPLs with absorption at 428 nm were obtained. These NPLs were thinner than the ones obtained at 140 °C as they were found to have a wider band gap.

### 3.2.2 Change in Confinement through Synthesis Method

One of the advantages of LHPs is that they can be synthesised through a variety of methods. This enables us to develop new methods or modify existing methods for synthesising LHPs of desired shape or size. Here I show CsPbBr<sub>3</sub> nanocrystals synthesised through hot injection method (2.3.8), a room temperature synthesis method (2.3.9), and a modified hot injection method (2.3.10), each resulting in the formation of nanoparticles of different shape/size.

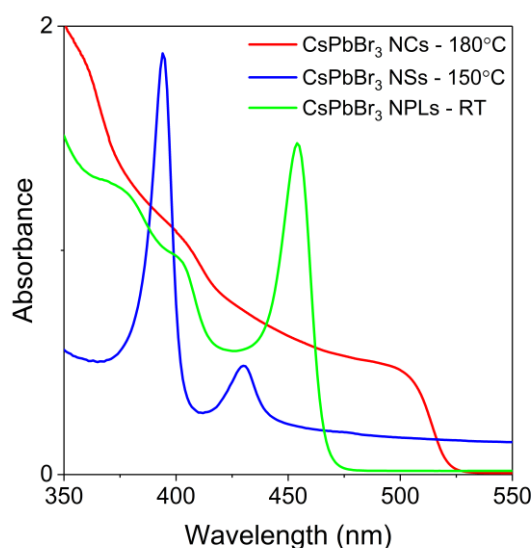


*Figure 3.4: Absorption spectra for CsPbBr<sub>3</sub> synthesised using 2.3.8, 2.3.9, and 2.3.10.*

CsPbBr<sub>3</sub> NCs with absorption at 500 nm were obtained using the standard hot injection method, while the room temperature synthesis method yielded CsPbBr<sub>3</sub> NPLs with absorption at 454 nm. The addition of OctAm and OctAc in the modified hot injection method resulted in the formation of two NPL species with absorption at 394 nm and 430 nm. These NPLs were different from the NPLs obtained through the room synthesis method. They were extremely thin (monolayer and bilayer thickness) in one dimension and large in the other two; hence, they have been named as nanosheets (NSs).

The NSs with absorption at 430 nm have the formula (OctAm)<sub>2</sub>[CsPbBr<sub>3</sub>]PbBr<sub>4</sub>. Octylamine binds to the perovskite at 'A' sites, and its long length prevents the perovskite from growing further, resulting in NSs of one perovskite layer (two PbBr layers). Monolayer thick NSs with incomplete perovskite structure are formed when octylamine binds to both sides of a single

PbBr layer, leaving no room for Cs. Such NSs are obtained in our case having absorption at 394 nm and have the formula  $(\text{OctAm})_2\text{PbBr}_4$  [4].

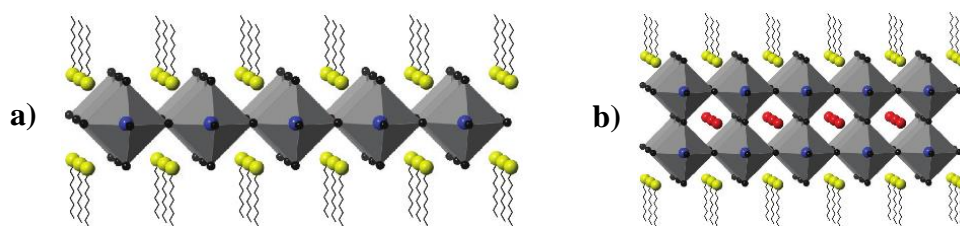


Figure 3.5: Structural representation of a)  $L_2\text{PbX}_4$  and b)  $L_2[\text{APbX}_3]\text{PbX}_4$  ( $L = \text{ligand}$ ).

Figures reproduced from [4].

### 3.2.3 Change in Band Gap through Mixing of Halides

Mixed halide perovskites were formed as alloys of lead bromide and lead iodide perovskites. Lead bromide perovskites have a wider band gap compared to lead iodide perovskites of similar same and size. Thus, alloying bromine in a lead iodide perovskite should increase the band gap or, in other words, alloying iodine in a lead bromide perovskite should decrease the band gap. I performed alloying by mixing  $\text{PbBr}_2$  and  $\text{PbI}_2$  together in desired proportion in the precursor solution while keeping the net Pb amount taken constant. I synthesised FABrI NCs (2.3.4),  $\text{CsPbBrI}$  NCs (2.3.8), and  $\text{CsPbBrI}$  NSs (2.3.10).

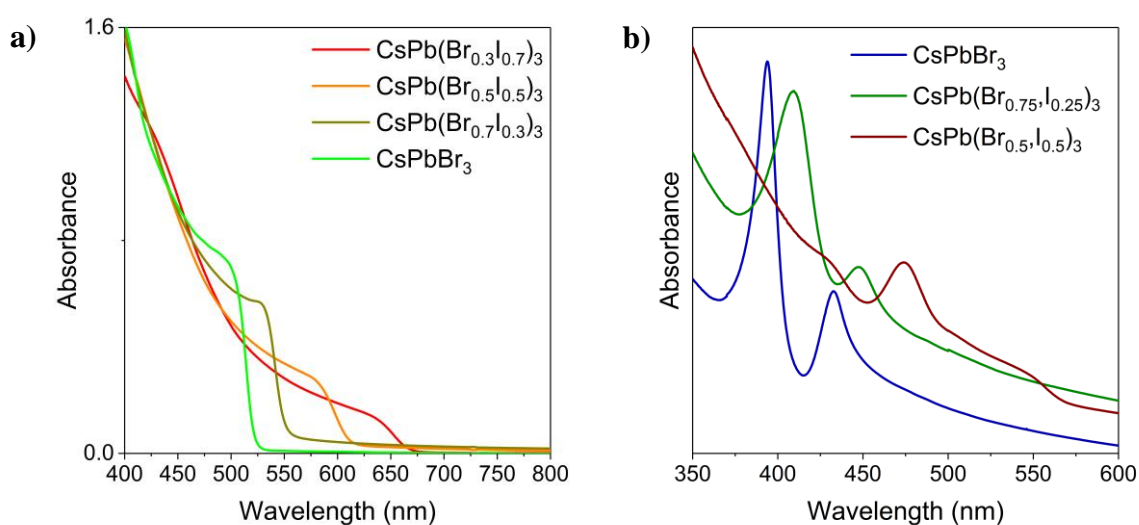


Figure 3.6: Absorption Spectra for a)  $\text{CsPbX}_3$  NCs synthesised using 2.3.8, and b)  $\text{CsPbX}_3$

NSs synthesised using 2.3.10.

It is evident from the absorption spectra that higher the bromine amount in the perovskite nanocrystal, wider is its band gap or, higher the iodine amount in the perovskite nanocrystal, narrower is its band gap. This holds true for the monolayer NSs which do not have an A site cation in their structure. Another thing worth noting is that lead iodide perovskites nanocrystals are formed at a lower temperature than lead bromide perovskites nanocrystals of similar morphology. Therefore, increasing the iodine content in the precursor might decrease the optimum temperature for the synthesis of perovskite of the desired shape/size. This can be seen in the spectrum of CsPb(Br<sub>0.5</sub>,I<sub>0.5</sub>)<sub>3</sub> NSs. The synthesis was done at 150 °C, which is the optimum temperature for the synthesis of CsPbBr<sub>3</sub> NSs. Addition of iodine reduced the optimum temperature, resulting in a lower yield of thin NSs and formation of NCs.

Absorption of individual materials is summarised in Table 3.1.

### 3.2.4 Change in Confinement through Reaction Precursor

I have already shown in 3.2.2 that adding straight ligands as precursors in hot injection method synthesis of CsPbBr<sub>3</sub> resulted in the formation of NSs instead of NCs or NPLs which could have formed at the lower temperature of synthesis if the extra ligands weren't added. In the room temperature synthesis of CsPbBr<sub>3</sub> NPLs, I added HBr to the beaker before the addition of bromide precursor and the product formed was different from the CsPbBr<sub>3</sub> NPLs without the addition of HBr.

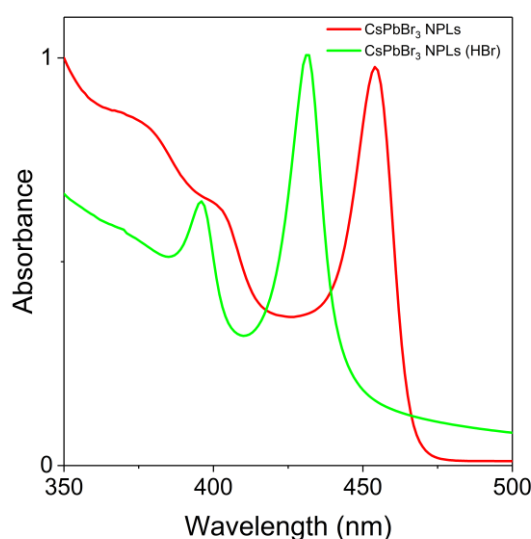


Figure 3.7: Absorption Spectra for CsPbBr<sub>3</sub> NPLs synthesised using 2.3.9.

In the unmodified synthesis, CsPbBr<sub>3</sub> NPLs with absorption at 454 nm were obtained. Whereas, after the addition of HBr, two NPLs species with absorption at 396 nm and 431 nm are obtained. These NPLs had the same band gap as the NSs obtained using 2.3.10, implying that the NPLs had similar monolayer and bilayer thickness. It has been hypothesised that HBr protonates the oleylamine to form oleylammonium cations which readily binds with the perovskite and hinders further growth, resulting in smaller NCs or thinner NPLs [26]. Although, to form NPLs of monolayer thickness, presence of straight ligands is required as straight ligands can bind to all the A sites which is not possible with the heavily bent structure of oleylamine. My hypothesis is that HBr performs addition reaction with the double bond of oleylamine to form 9-Br-octadecylamine. The removal of double bond straightens the ligand, which then causes the formation of the monolayer NPLs.

### 3.2.5 Summary

The LHPs of different size, shape and composition synthesised have been summarised below with their absorption to show the variations in the band gap.

*Table 3.1: Absorption of LHPs of different size, shape and composition (L represents the straight ligands octylamine or the hypothesised 9-Br-octadecylamine)*

<u>Formula</u>	<u>Shape</u>	<u>Absorption</u>	
		nm	eV
FAPbI <sub>3</sub>	NC	754	1.64
FAPb(Br <sub>0.2</sub> ,I <sub>0.8</sub> ) <sub>3</sub>	NC	735	1.69
FAPb(Br <sub>0.4</sub> ,I <sub>0.6</sub> ) <sub>3</sub>	NC	781	1.59
FAPbBr <sub>3</sub>	Small NC	492	2.52
FAPbBr <sub>3</sub>	NPL	428-433	2.86-2.90
CsPbBr <sub>3</sub>	NC	500	2.48
CsPbBr <sub>3</sub>	NPL	454	2.73
CsPbBr <sub>3</sub>	Thin NPL	430	2.89
CsPbBr <sub>3</sub>	Thick NPL	482	2.57
CsPb(Br <sub>0.7</sub> ,I <sub>0.3</sub> ) <sub>3</sub>	NC	527	2.35
CsPb(Br <sub>0.5</sub> ,I <sub>0.5</sub> ) <sub>3</sub>	NC	579	2.14

$\text{CsPb}(\text{Br}_{0.5}, \text{I}_{0.5})_3$	Small NC	551	2.25
$\text{CsPb}(\text{Br}_{0.3}, \text{I}_{0.7})_3$	NC	635	1.95
$\text{L}_2[\text{CsPbBr}_3]\text{PbBr}_4$	NS	430-431	2.88
$\text{L}_2[\text{CsPb}(\text{Br}_{0.75}, \text{I}_{0.25})_3]\text{Pb}(\text{Br}_{0.75}, \text{I}_{0.25})_4$	NS	447	2.77
$\text{L}_2[\text{CsPb}(\text{Br}_{0.5}, \text{I}_{0.5})_3]\text{Pb}(\text{Br}_{0.5}, \text{I}_{0.5})_4$	NS	474	2.62
$\text{L}_2\text{PbBr}_4$	NS	394-396	3.13-3.15
$\text{L}_2\text{Pb}(\text{Br}_{0.75}, \text{I}_{0.25})_4$	NS	409	3.03
$\text{L}_2\text{Pb}(\text{Br}_{0.5}, \text{I}_{0.5})_4$	NS	432	2.87

### 3.3 Charge Transport Properties of FAPI

Interdigitated electrodes are two sets of long electrodes in a fork-in-fork type assembly in which electrodes within each set are connected to a common pad, but there is no connection between electrodes from different sets. When a film of perovskite nanocrystals is deposited on the electrodes, it acts as the connecting medium between the two sets. When the voltage bias is applied between the two sets, a charge flow is established through the film.

#### 3.3.1 Processing of the Perovskites Film

The quality of the deposited film of perovskites is very crucial while studying the transport properties of perovskites. Two common ways of preparing films of perovskites nanocrystals are dropcasting (2.4.2) and spin-coating (2.4.3). Dropcasted films are usually thick and uneven, as there is no thickness control, whereas spin-coated films are thinner and of uniform thickness. Spin-coating is preferred for film preparation as spin-coated films are of higher quality. Although, spin-coating results in loss of material and therefore, should not be used if the material is precious. To form good quality films by spin-coating, the material needs to be colloidal stable in the solvent. So, films of larger particles such as NPLs and nanorods, which have low colloidal stability, cannot be prepared using spin-coating without quality issues. FAPI NCs, PbS CQDs, and FAPI-PbS hybrid are stable in toluene and, hence, spin-coating is used to prepare good quality films of them.

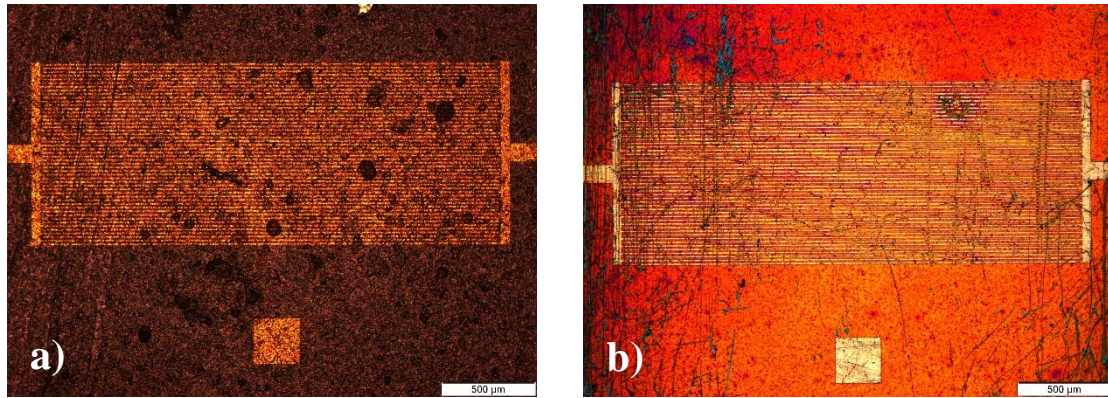


Figure 3.8: Microscopic images of interdigitated electrodes with a) dropcasted film of  $\text{CsPbBr}_3$  NSs and b) spin-coated film of  $\text{CsPb}(\text{Br}_{0.5}\text{I}_{0.5})_3$  NCs.

Another important factor affecting the transport properties of perovskite nanoparticles is ligands. Ligands bind to the surface of the colloidal nanocrystals protecting them from the environment and providing stability. But they also act as tunnel barriers for charge carriers. The width of the tunnel barrier is equal to the length of ligand between two perovskite nanoparticles. Longer ligands such as oleylamine and oleate hamper the charge transport in the film by a great degree. Therefore, they are exchanged by the shorter acetate ligand to reduce the tunnel barrier effect. Ligand exchange occurs in films as a diffusion process where the long ligands percolate out of the film and the short ligands percolate in. Ligand exchange becomes crucial when the perovskite nanocrystals are used to form a solar cell as ligands slow down the charge transfer between nanocrystals and charge carrier accepting layers [27].

Two things should be kept in mind for ligand exchange. Ligand exchange only occurs in the top few layers of the film, and so, if the film is thick, the bottom part of it (which is in touch with the electrodes) still contains long ligands rendering the ligand exchange ineffective. Therefore, the thickness of the film should be less (typically less than 50 nm) for ligand exchange. Exchange of long ligand molecules with short ones causes cracks in the film. Spin-coating the perovskite material again on the ligand exchanged film fills in these cracks and also adds material to the film. The film gets crosslinked after ligand exchange due to shorter ligands and, hence, does not get dissolved when more material is added. Ligand exchange can then be performed again on the new layer. Multiple spin-coating and subsequent ligand exchange steps are done to build a high-quality film of appreciable thickness while having short ligands.

### 3.3.2 Transport in FAPI Films

FAPI films were prepared on interdigitated electrodes as described above. I-V characteristics of this device were measured in dark and under illumination from a 405 nm laser. An Ohmic response was observed implying that the voltage bias applied wasn't enough to excite electrons. The current was due to movement of free charge carriers already present in the bands due to excitation of electrons by radiation.

Under dark conditions, there is no radiation to excite electrons and generate free charge carriers; still a current is observed. This dark current is due to thermally activated generation-recombination of electrons and holes and drifting of charge carriers from one nanocrystal to another [28]. The dark current is dependent on available carrier concentration which increases with decrease in the band gap. Defects also lead to an increase in carrier concentration. FAPI has a defect tolerant structure, and a wider band gap compared to infrared absorbing II-VI or IV-VI semiconductors such as PbS and therefore, has a much lower carrier concentration. As a result, the dark current in FAPI films is much lower than that in PbS films.

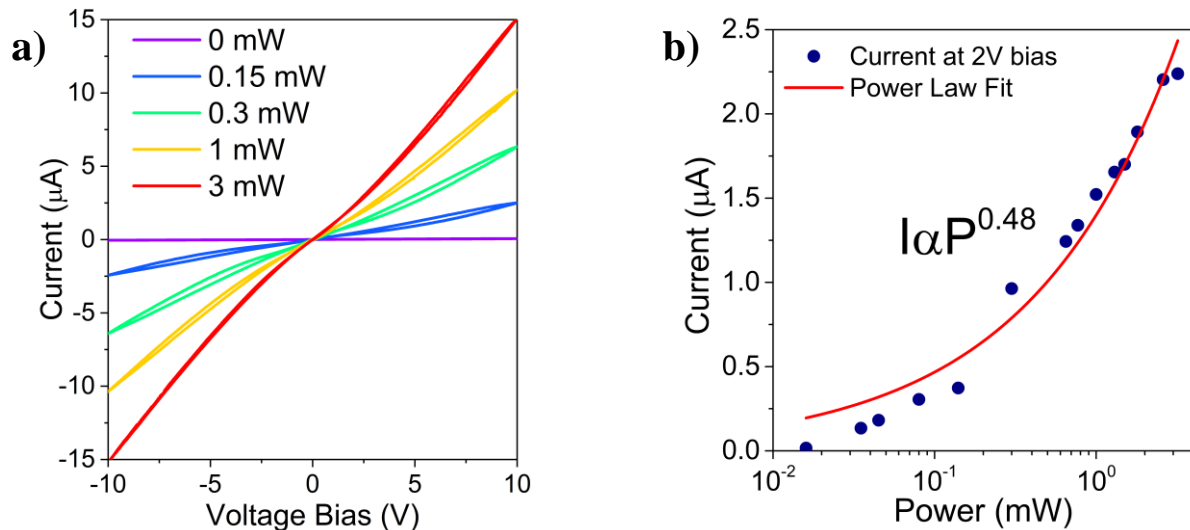
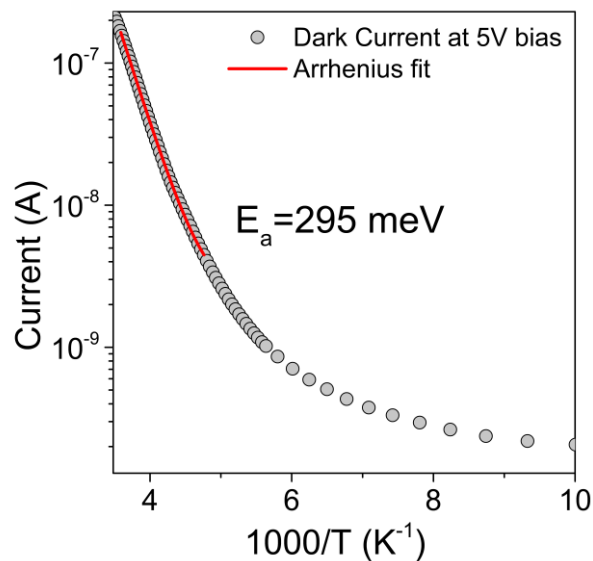


Figure 3.9: a) I-V curves of FAPI NCs film under different illumination power, b) Photocurrent dependence on incident power in FAPI NCs film.

FAPI NCs film was illuminated with a 405 nm laser which is well above the 1.6 eV band gap of FAPI NCs. A significant increase in current was observed, which increased further with increase in the laser power. When the perovskites film is illuminated by a light of energy greater

than the band gap of the material, electrons are excited from the valence band to the conduction band, increasing the availability of the charge carriers and consequently, the current through the device. This enhanced current is called photocurrent as it is induced by photons. Increasing the power of the incident light causes excitation of more electrons and increases the photocurrent due to the generation of more charge carriers. This way, the perovskites film deposited on interdigitated electrodes works as a photodetector.

The photocurrent in FAPI NCs film was plotted as a function of the incident light power, and a trend was observed. The plot was fitted with a power law equation  $I = cP^x$ , where  $I$  is the photocurrent,  $P$  is the incident power, and  $c$  is a constant. The exponent  $x$  came out to be approximately 0.5. This is suggestive of the fact that the charge carrier generation in FAPI is limited by band-to-band recombination, which is a bimolecular process, and not by trapping of charge carriers on surface induced traps, which is a monomolecular process [29]. This is another evidence that the FAPI band gap is free of trap states.



*Figure 3.10: Arrhenius plot of photocurrent v/s temperature of the film.*

The FAPI NCs film was cooled down, and the dark current was measured as a function of the temperature of the film. A drop in the dark current was observed as the temperature decreased. This is due to the reduction in thermally excited electrons with decreasing temperature. This suggests that the transport in the FAPI NCs film, driven by hopping of charge carriers from band to band, is dependent on the thermal activation energy of the carriers in the dark. The

photocurrent vs temperature plot was fitted with the Arrhenius equation to determine the thermal activation which was calculated as 295 meV.

Arrhenius equation-  $I = Ae^{-E_a/k_B T}$ , where I is the measured dark current, A is the Arrhenius factor,  $E_a$  is the thermal activation energy,  $k_B$  is the Boltzmann constant, and T is the measured sample temperature in Kelvins.

The thermal activation energy is always smaller than the energy gap between the Fermi level and bands, which implied that the Fermi level in FAPI NCs was away from both valence and conduction bands by at least 295 meV. The location of the Fermi level deep within the band gap also showed the absence of trap states in FAPI NCs.

The data presented in this section has been published in [30].

### 3.4 Mixing FAPI and PbS

PbS CQD solar cells suffer from low power conversion efficiency and high dark current. FAPI NCs overcome both of these problems due to their defect tolerance and wider band gap, but lack behind PbS CQDs in absorption of SWIR. FAPI NCs and PbS CQDs were mixed in different proportions to form hybrids, so that both IR absorption property of PbS and the low dark current and the defect tolerance properties of FAPI could be combined. Absorption spectra and TEM images were taken to study the structure of the FAPI-PbS hybrids containing different amounts of PbS.

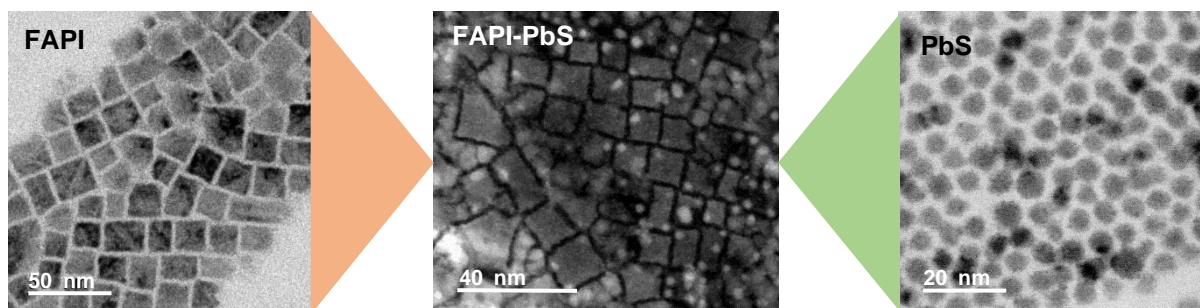


*Figure 3.11: TEM images of FAPI NCs, PbS CQDs, and FAPI-PbS hybrid.*

The PbS CQDs had an absorption peak at 1.5  $\mu\text{m}$ , and the FAPI NCs had a bulk like absorption at 750 nm. The absorption spectra of FAPI-PbS hybrids showed an absorption around 1.5  $\mu\text{m}$ , which comes from PbS, and a change in slope around 750 nm, which corresponds to FAPI. This suggests that both FAPI and PbS had not undergone any structural change during mixing. TEM images showed that the cubical shaped FAPI and the spherical shaped PbS remained intact during the mixing. The TEM image of the FAPI-PbS hybrid showed small spherical QDs of PbS spread over the cubical array of FAPI NCs, which was an evidence of mixing of the two materials at the nanoscale level.

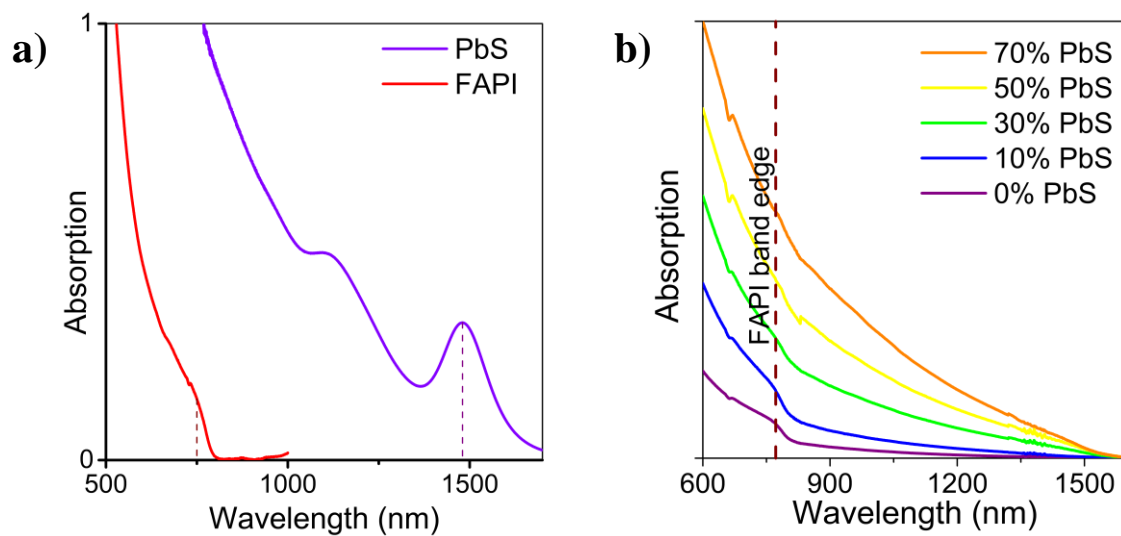


Figure 3.12: Absorption spectra of a) separate FAPI and PbS and b) FAPI-PbS hybrids.

The aim was to have a material which can absorb in infrared while maintaining the favourable transport properties associated with LHPs. Two factors were kept in mind while selecting the right proportion of FAPI and PbS-

- 1) The ratio of PbS should be enough to have a good amount of IR absorption. This was ensured by observing the increase in photocurrent under illumination by a 1.55  $\mu\text{m}$  laser.
- 2) The ratio of FAPI should be enough to not cross the percolation threshold of PbS so that the transport of charge carriers is driven by FAPI, and not by PbS. FAPI NCs have a wider band gap compared to PbS CQDs, and therefore, a reduced dark current is observed with FAPI driven transport compared to the transport through PbS.

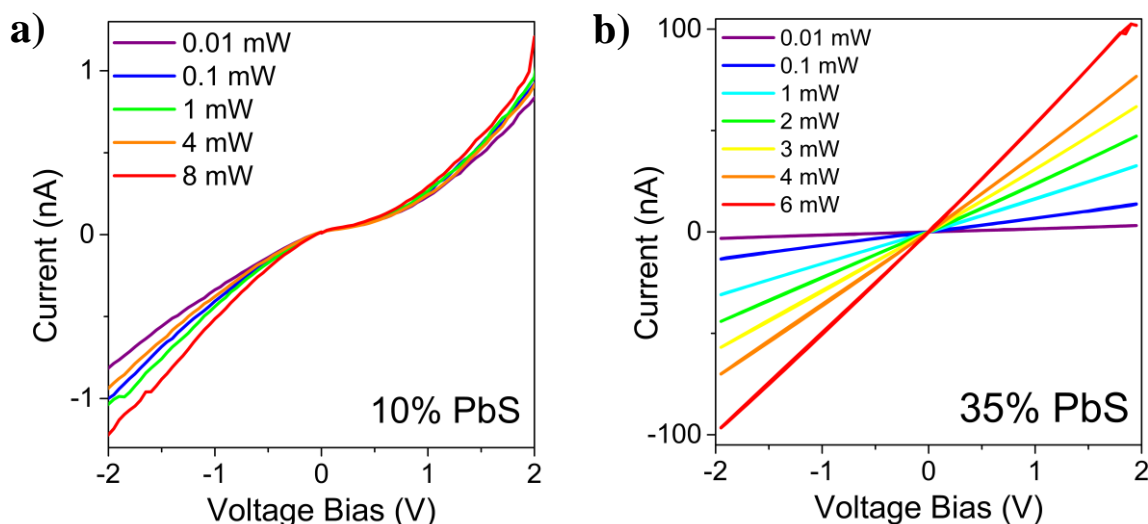


Figure 3.13: Photocurrent dependence on incident power in films of a) 10% PbS FAPI-PbS hybrid and b) 35% PbS FAPI-PbS hybrid.

Films of PbS CQDs and FAPI-PbS hybrids having different amount of PbS were deposited on interdigitated electrodes in a similar fashion as for films of FAPI NCs. I-V characteristics of these films were measured in dark and under illumination from a 1.55  $\mu\text{m}$  laser. The laser power was varied, and change in photocurrent was observed. Little to no increase in photocurrent was observed in the 10% PbS FAPI-PbS hybrid on increasing the illumination power (Figure 3.13a), indicating that the IR light from the laser was not being absorbed well enough by the material. When the PbS amount was increased to 35%, the photosensitivity of the hybrid to IR increased significantly (Figure 3.13b), indicating that the IR light was being absorbed by the material and was causing generation of charge carriers. Therefore, FAPI-PbS hybrid with 35% PbS or more was considered to be a good IR absorber with the threshold lying somewhere between 10% and 35%.

To confirm that the photocurrent response was induced by the absorption of IR by PbS, photocurrent spectra were taken for all the films using an FTIR spectroscopy instrument (2.6.3). An increase in the IR photoconduction in the films was observed with increase in the PbS amount in the FAPI-PbS hybrid, suggesting that the IR absorption by PbS was indeed responsible for the photocurrent in the film.

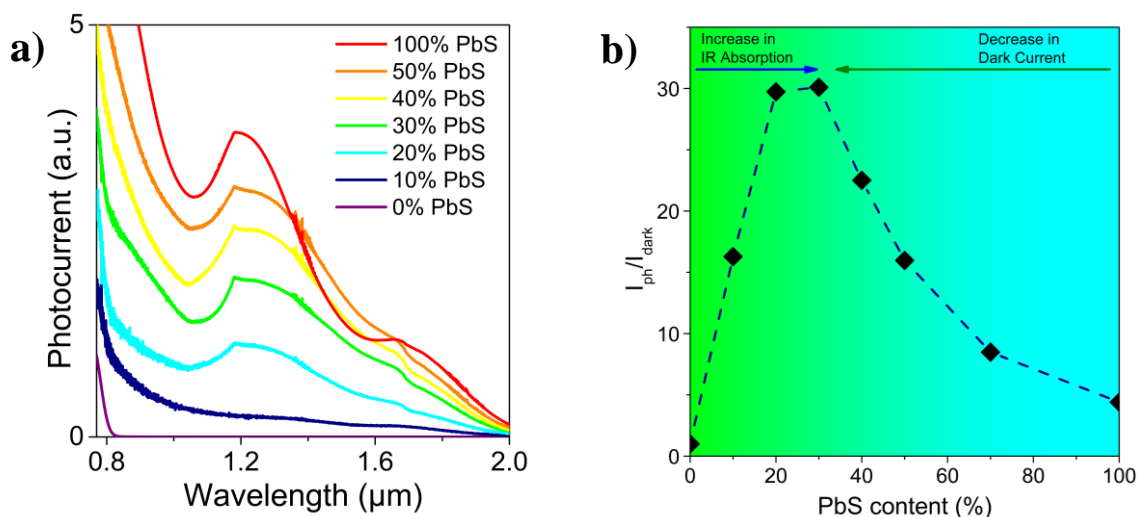


Figure 3.14: a) Photocurrent spectra for films of FAPI-PbS hybrids and b) Ratio of photocurrent and dark current plotted against PbS content present in the FAPI-PbS hybrids.

The photocurrent to dark current ratio was measured for each FAPI-PbS hybrid having different PbS amount at a fixed laser power. It was observed that when FAPI is introduced into PbS, a reduction in dark current was observed, which is due to the wider band gap of FAPI. A decrease in photocurrent was also observed due to reduced absorption of IR light although, the drop in photocurrent was much less pronounced compared to the drop in dark current. At low PbS concentration, it was observed that while the dark current was low, the photocurrent was also very weak due to poor absorption of IR light, resulting in a poor photo to dark current ratio. This ratio improved as PbS amount was increased. At the interface of these two regimes, the photo to dark current was maximised, giving the optimal amount of PbS doping in the FAPI-PbS hybrid at 35%.

35% PbS FAPI-PbS hybrid was found to be the optimal material showing IR absorption along with perovskite driven transport.

### 3.5 XPS Measurements

XPS measurements were done of films of FAPI NCs, PbS CQDs, and 35% PbS FAPI-PbS hybrid to identify their electronic structures. The films were prepared on a gold substrate in the same way as they were prepared for transport measurements (2.5.4). A gold substrate was used instead of Si/SiO<sub>2</sub> wafer to avoid charging effect on the sample due to the insulating substrate.

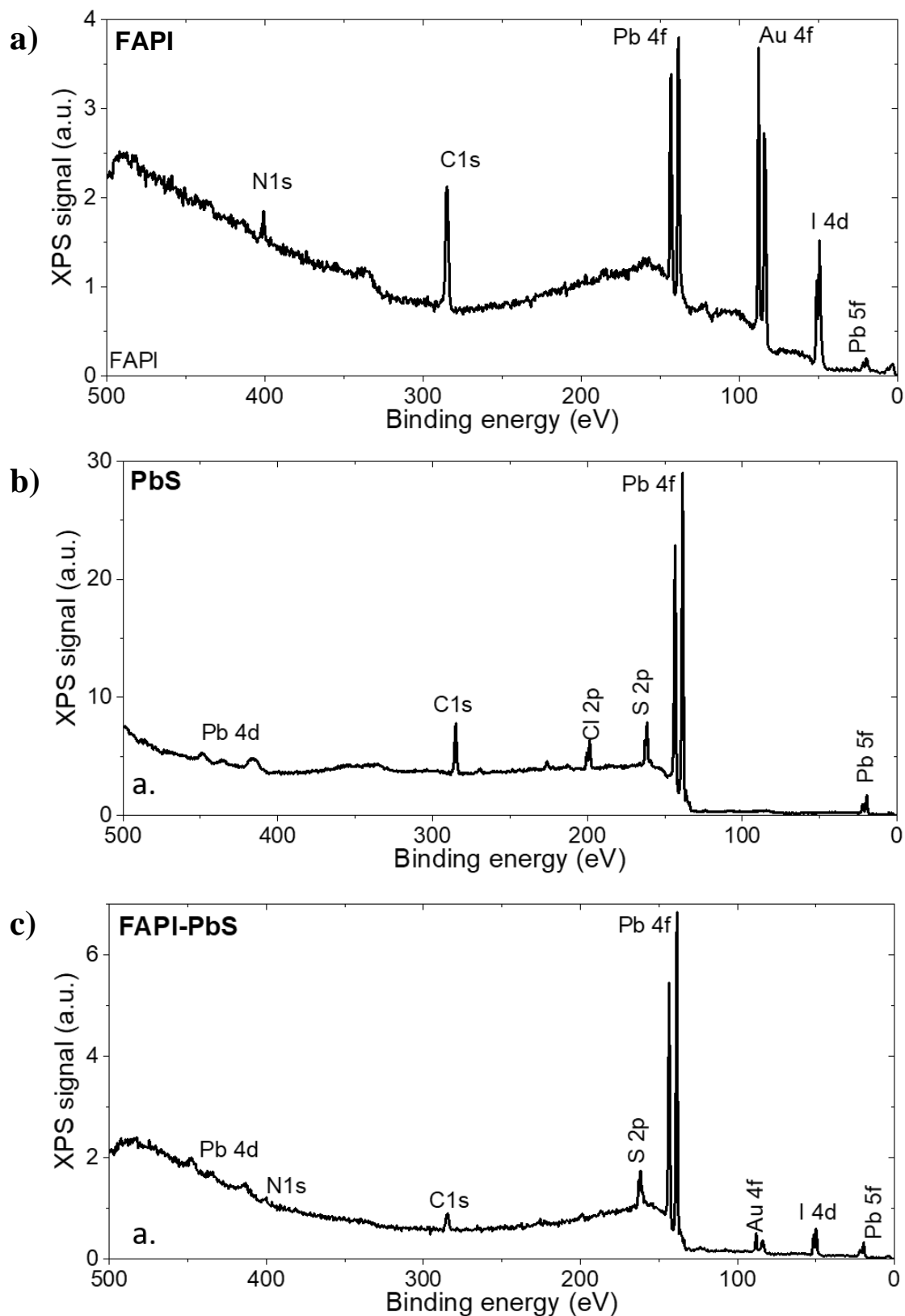


Figure 3.15: XPS spectra for a) FAPI NCs, b) PbS CQDs, and c) 35% PbS FAPI-PbS hybrid showing core level peaks for elements present in FAPI and PbS. Au peak is from the substrate.

In XPS, X-rays are used to excite electrons from the surface of the sample to the vacuum, and then their kinetic energy is measured. The binding energy of the electron is then calculated as  $B.E. = h\nu - K.E. - W_{f-ana}$ , where  $h\nu$  is the energy of the incident X-rays,  $K.E.$  is the measured kinetic energy of the photoelectrons, and  $W_{f-ana}$  is the workfunction of the analyser. In our case, X-rays of 600 eV were used which had enough energy to excite the electrons bound to the core levels of outer shells of the atoms. When this happened, a peak was observed in the spectrum corresponding to the binding energy of the electrons to the core level. The binding energy at a particular core level of an element is fairly constant and only shifts slightly depending on the oxidation state and chemical environment. All the electron binding energies detectable by XPS have been well documented and compiled in several databases. The database used for identifying peaks in this case was [31].

XPS spectrum of FAPI NCs showed the core level peaks for Pb, I, C, and N. The C and N peaks came from two sources, FA and the ligands. In the PbS CQDs XPS spectrum, peaks for Pb, S, Cl, and C were visible. The C peak came from the ligands while the Cl peak came from the  $PbCl_2$  precursor. The XPS spectrum of 35% PbS FAPI-PbS hybrid contained all the peaks corresponding to the elements of FAPI NCs and PbS CQDs.

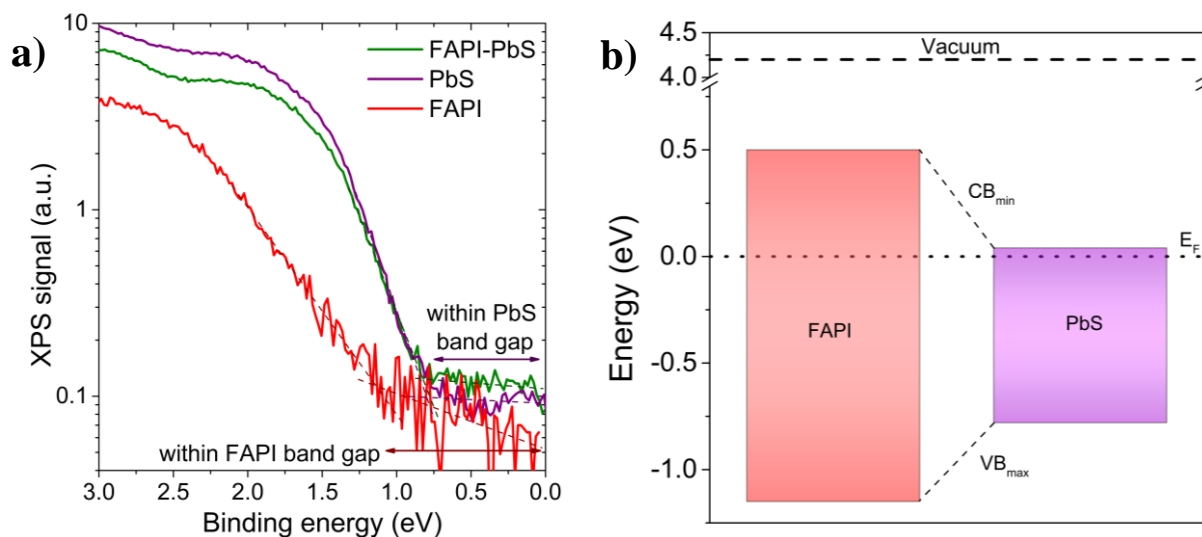


Figure 3.16: a) Valence bands of FAPI NCs, PbS CQDs, and 35% PbS FAPI-PbS hybrid, and b) band gap structures of FAPI NCs (red) and PbS CQDs (purple).

XPS spectrum was used to identify the valence bands of the three nanomaterials (Figure 3.16a). The valence band was identified by a sharp reduction in the emission of photoelectrons of

higher kinetic energy. The valence band of 35% PbS FAPI-PbS hybrid was found to correspond to the PbS CQDs. The position of Au Fermi level ( $E_F$ ) was fixed at zero and position of valence band ( $VB_{max}$ ) was measured corresponding to it ( $VB_{max} - E_F$ ). This value was found to be 1.15 eV for FAPI NCs and 0.78 eV for PbS CQDs. Since the band gaps for both FAPI NCs and PbS CQDs were known, the complete band gap picture could be drawn (Figure 3.16b). For PbS CQDs, the Fermi level was very close to the conduction band, making it behave like a quasi-n-type degenerate semiconductor [32]. In FAPI, the Fermi level was found to be slightly towards the conduction band, which could be due to fluctuations from sample to sample. A type-I band alignment was found to exist between FAPI and PbS. The  $VB_{max} - E_F$  value was 0.83 eV for 35% PbS FAPI-PbS hybrid which could be due to slight downward bending of PbS valence band. XPS was also used to measure the electronic work function ( $W_f$ ). The cutoff value for photoelectron emission, i.e., position of 0 eV emission was determined with respect to the Fermi level and subtracted from the photon energy to get  $W_f$ . For FAPI NCs,  $W_f$  was 4.21 eV, and for PbS CQDs,  $W_f$  was 4.15 eV.

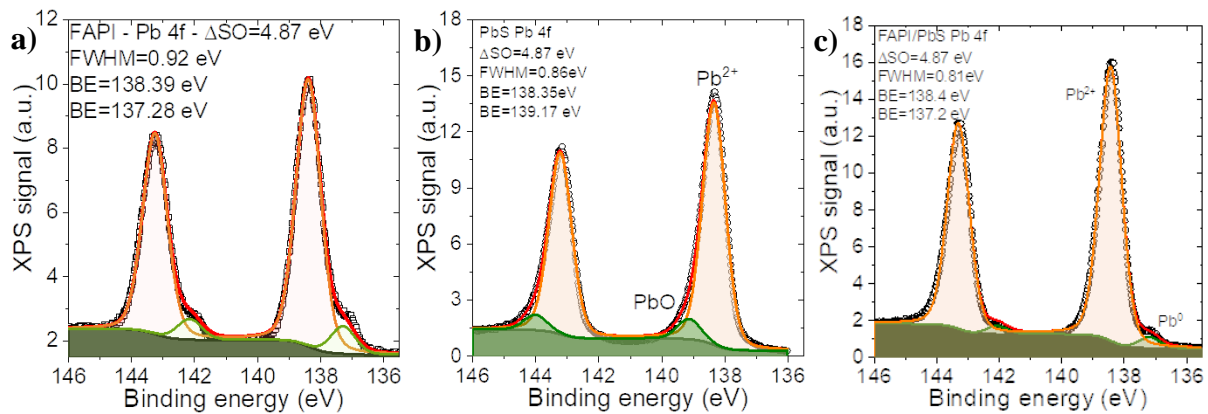


Figure 3.17: Fitted core level peaks of Pb 4f in a) FAPI NCs, b) PbS CQDs, and c) 35% PbS FAPI-PbS hybrid.

XPS spectra were zoomed in on core level peaks and were fitted to identify all the individual peaks and the corresponding binding energies. The investigation on Pb 4f peaks is presented here. In FAPI NCs, a large contribution of  $Pb^{2+}$  and a small contribution from  $Pb^0$  were observed. In PbS CQDs, a large contribution of  $Pb^{2+}$  coming from PbS and a small contribution of  $Pb^{2+}$  coming from PbO, which was present as an oxide shell, were observed. The higher electronegativity of oxygen shifted the peak towards an apparent higher oxidation state. In 35% PbS FAPI-PbS hybrid, a large contribution of  $Pb^{2+}$  and a small contribution from  $Pb^0$  were

observed. The PbO peak was not seen owing to the low amount of PbS. No new peaks and no peak shifts were observed in the case of 35% PbS FAPI-PbS hybrid, indicating that the integrity of FAPI NCs and PbS CQDs was preserved, and that there is no charge transfer between the two in the dark.

## CHAPTER 4

### CONCLUSION

#### 4.1 Summary

Quantum confinement effect has been studied in LHPs. Increase in band gap with decrease in size of nanocrystals was observed. Band separation was observed by the introduction of strong confinement in one direction of the nanoparticles.

Two phases of FAPI were identified using powder X-ray diffraction. Formation of cubic bulk-like nanocrystals was confirmed using TEM images. I-V characteristics of FAPI NCs film deposited on Au interdigitated electrodes (fabricated in the INSP cleanroom) were studied, and an Ohmic response was observed. It was illuminated with a 405 nm laser of varying power. High photocurrent to dark current ratio was obtained, and the photocurrent was found to be dependent on the illumination power with a power law exponent of 0.5, indicative of band-to-band recombination. Arrhenius fit was done on dark current as a function of temperature, and the thermal activation energy was found to be 295 meV, indicative of the fact that the Fermi level sits deep within the band. Both these observations are evidence that the band gap of FAPI is trap free.

A hybrid material was formed by mixing FAPI NCs and PbS CQDs. Absorption spectra and TEM images showed the both FAPI and PbS were intact in the hybrid, and PbS spheres were uniformly dispersed all over the FAPI NC array. Transport in the films of hybrid material was studied using a 1.55  $\mu\text{m}$  laser diode to find the PbS doping amount resulting in the maximum photocurrent to dark current ratio. Photocurrent spectra showed that the enhancement of photocurrent was due to IR absorption by PbS and wider FAPI band gap meant reduced dark current in FAPI driven transport. 35% PbS was identified as the optimal PbS doping amount as the hybrid had both IR absorption and transport properties of FAPI.

XPS measurements (done at the SOLEIL Synchrotron facility) showed that PbS CQDs were quasi n-type degenerate due to closeness of Fermi level to the conduction band. The band alignment between FAPI and PbS was found to be a Type-I. No core level peak shifts were

observed in the 35% PbS FAPI-PbS hybrid, indicating intact structures of both FAPI NCs and PbS CQDs and no charge transfer between them in dark conditions.

## **4.2 Future Outlook**

The new hybrid material shows promising applications in solar cells as it absorbs majority of the solar spectrum and enjoys the benefits associated with LHPs. Further studies have already been done on this material by the OCN group. FET was made, which showed an n-type behaviour. To compensate for the reduced IR absorption of the material, it was deposited on GMR electrodes which enhances absorption by multiple reflections within the device [33]. This device shows a much higher signal-to-noise ratio and a faster time response compared to PbS CQD device. This material opens new horizons for infrared optoelectronics which can now benefit from the defect tolerance of perovskites.

## REFERENCES

- [1] S. V. Gaponenko, *Optical Properties of Semiconductor Nanocrystals* (Cambridge University Press, Cambridge, 1998).
- [2] C. De Mello Donegá, *Nanoparticles: Workhorses of nanoscience* (Springer-Verlag Berlin Heidelberg, 2014).
- [3] M. Borowski, *Perovskites: Structure, properties and uses* (Nova Science Publishers Inc., 2010).
- [4] M. C. Weidman, M. Seitz, S. D. Stranks and W. A. Tisdale, *Highly Tunable Colloidal Perovskite Nanoplatelets through Variable Cation, Metal, and Halide Composition*, ACS Nano **10**, 7830-7839 (2016).
- [5] L. Pan and G. Zhu, *Perovskite Materials - Synthesis, Characterisation, Properties, and Applications* (InTechOpen, 2016).
- [6] G. H. Carey, A. L. Abdelhady, Z. Ning, S. M. Thon, O. M. Bakr and E. H. Sargent, *Colloidal Quantum Dot Solar Cells*, Chemical Reviews **115**, 12732-12763 (2015).
- [7] H. Huang, M. I. Bodnarchuk, S. V. Kershaw, M. V. Kovalenko and A. L. Rogach, *Lead Halide Perovskite Nanocrystals in the Research Spotlight: Stability and Defect Tolerance*, ACS Energy Letters **2**, 2071-2083 (2017).
- [8] L. Protesescu, S. Yakunin, M. I. Bodnarchuk, F. Krieg, R. Caputo, C. H. Hendon, R. X. Yang, A. Walsh and M. V. Kovalenko, *Nanocrystals of Cesium Lead Halide Perovskites (CsPbX<sub>3</sub>, X = Cl, Br, and I): Novel Optoelectronic Materials Showing Bright Emission with Wide Color Gamut*, Nano Letters **15**, 3692-3696 (2015).
- [9] E. Lhuillier, S. Pedetti, S. Ithurria, B. Nadal, H. Heuclin and B. Dubertret, *Two-Dimensional Colloidal Metal Chalcogenides Semiconductors: Synthesis, Spectroscopy, and Applications*, Accounts of Chemical Research **48**, 22-30 (2015).
- [10] F. Wang, Y. Wang, Y.-H. Liu, P. J. Morrison, R. A. Loomis and W. E. Buhro, *Two-Dimensional Semiconductor Nanocrystals: Properties, Templated Formation, and Magic-Size Nanocluster Intermediates*, Accounts of Chemical Research **48**, 13-21 (2015).
- [11] R. Quintero-Bermudez, A. Gold-Parker, A. H. Proppe, R. Munir, Z. Yang, S. O. Kelley, A. Amassian, M. F. Toney and E. H. Sargent, *Compositional and orientational control in metal halide perovskites of reduced dimensionality*, Nature Materials **17**, 900-907 (2018).
- [12] C. Tablero Crespo, *The effect of the halide anion on the optical properties of lead halide perovskites*, Solar Energy Materials and Solar Cells **195**, 269-273 (2019).

- [13] F. F. Targhi, Y. S. Jalili and F. Kanjouri, *MAPbI<sub>3</sub> and FAPbI<sub>3</sub> perovskites as solar cells: Case study on structural, electrical and optical properties*, Results in Physics **10**, 616-627 (2018).
- [14] P. Tonui, S. O. Oseni, G. Sharma, Q. Yan and G. Tessema Mola, *Perovskites photovoltaic solar cells: An overview of current status*, Renewable and Sustainable Energy Reviews **91**, 1025-1044 (2018).
- [15] T. C. Jellicoe, J. M. Richter, H. F. J. Glass, M. Tabachnyk, R. Brady, S. E. Dutton, A. Rao, R. H. Friend, D. Credgington, N. C. Greenham and M. L. Böhm, *Synthesis and Optical Properties of Lead-Free Cesium Tin Halide Perovskite Nanocrystals*, Journal of the American Chemical Society **138**, 2941-2944 (2016).
- [16] L. Protesescu, S. Yakunin, S. Kumar, J. Bär, F. Bertolotti, N. Masciocchi, A. Guagliardi, M. Grotevent, I. Shorubalko, M. I. Bodnarchuk, C.-J. Shih and M. V. Kovalenko, *Dismantling the “Red Wall” of Colloidal Perovskites: Highly Luminescent Formamidinium and Formamidinium–Cesium Lead Iodide Nanocrystals*, ACS Nano **11**, 3119-3134 (2017).
- [17] D. Yu, F. Cao, Y. Gao, Y. Xiong and H. Zeng, *Room-Temperature Ion-Exchange-Mediated Self-Assembly toward Formamidinium Perovskite Nanoplates with Finely Tunable, Ultrapure Green Emissions for Achieving Rec. 2020 Displays*, Advanced Functional Materials **28**, 1800248 (2018).
- [18] M. Fu, P. Tamarat, J.-B. Trebbia, M. I. Bodnarchuk, M. V. Kovalenko, J. Even and B. Lounis, *Unraveling exciton–phonon coupling in individual FAPbI<sub>3</sub> nanocrystals emitting near-infrared single photons*, Nature Communications **9**, 3318 (2018).
- [19] I. Moreels, Y. Justo, B. De Geyter, K. Haustraete, J. C. Martins and Z. Hens, *Size-Tunable, Bright, and Stable PbS Quantum Dots: A Surface Chemistry Study*, ACS Nano **5**, 2004-2012 (2011).
- [20] Q. A. Akkerman, S. G. Motti, A. R. Srimath Kandada, E. Mosconi, V. D’Innocenzo, G. Bertoni, S. Marras, B. A. Kamino, L. Miranda, F. De Angelis, A. Petrozza, M. Prato and L. Manna, *Solution Synthesis Approach to Colloidal Cesium Lead Halide Perovskite Nanoplatelets with Monolayer-Level Thickness Control*, Journal of the American Chemical Society **138**, 1010-1016 (2016).
- [21] W. J. Mir, C. Livache, N. Goubet, B. Martinez, A. Jagtap, A. Chu, N. Coutard, H. Cruguel, T. Barisien, S. Ithurria, A. Nag, B. Dubertret, A. Ouerghi, M. G. Silly and E. Lhuillier, *Strategy to overcome recombination limited photocurrent generation in CsPbX<sub>3</sub> nanocrystal arrays*, Applied Physics Letters **112**, 113503 (2018).

- [22] Y. Liu, M. Siron, D. Lu, J. Yang, R. dos Reis, F. Cui, M. Gao, M. Lai, J. Lin, Q. Kong, T. Lei, J. Kang, J. Jin, J. Ciston and P. Yang, *Self-Assembly of Two-Dimensional Perovskite Nanosheet Building Blocks into Ordered Ruddlesden–Popper Perovskite Phase*, *Journal of the American Chemical Society* **141**, 13028-13032 (2019).
- [23] N. Pellet, P. Gao, G. Gregori, T.-Y. Yang, M. K. Nazeeruddin, J. Maier and M. Grätzel, *Mixed-Organic-Cation Perovskite Photovoltaics for Enhanced Solar-Light Harvesting*, *Angewandte Chemie International Edition* **53**, 3151-3157 (2014).
- [24] C. C. Stoumpos, C. D. Malliakas and M. G. Kanatzidis, *Semiconducting Tin and Lead Iodide Perovskites with Organic Cations: Phase Transitions, High Mobilities, and Near-Infrared Photoluminescent Properties*, *Inorganic Chemistry* **52**, 9019-9038 (2013).
- [25] V. K. Ravi, A. Swarnkar, R. Chakraborty and A. Nag, *Excellent green but less impressive blue luminescence from CsPbBr<sub>3</sub> perovskite nanocubes and nanoplatelets*, *Nanotechnology* **27**, 325708 (2016).
- [26] R. Qu, L. Zou, X. Qi, C. Liu, W. Zhao, J. Yan, Z. Zhang and Y. Wu, *Changing the shape and optical properties of CsPbBr<sub>3</sub> perovskite nanocrystals with hydrohalic acids using a room-temperature synthesis process*, *CrystEngComm* **22**, 1853-1857 (2020).
- [27] Q. Shang, B. D. Piercy, M. D. Losego and T. Lian, *Effect of Surface Ligand on Charge Separation and Recombination at CsPbI<sub>3</sub> Perovskite Quantum Dot/TiO<sub>2</sub> Interfaces*, *The Journal of Physical Chemistry C* **123**, 21415-21421 (2019).
- [28] B. T. Marozas, W. D. Hughes, X. Du, D. E. Sidor, G. R. Savich and G. W. Wicks, *Surface dark current mechanisms in III-V infrared photodetectors [Invited]*, *Optical Materials Express* **8**, 1419-1424 (2018).
- [29] L. J. Willis, J. A. Fairfield, T. Dadosh, M. D. Fischbein and M. Drndic, *Controlling Nanogap Quantum Dot Photoconductivity through Optoelectronic Trap Manipulation*, *Nano Letters* **9**, 4191-4197 (2009).
- [30] D. Amelot, P. Rastogi, B. Martinez, C. Gréboval, C. Livache, F. A. Bresciani, J. Qu, A. Chu, M. Goyal, S.-S. Chee, N. Casaretto, X. Z. Xu, C. Méthivier, H. Cruguel, A. Ouerghi, A. Nag, M. G. Silly, N. Witkowski and E. Lhuillier, *Revealing the Band Structure of FAPI Quantum Dot Film and Its Interfaces with Electron and Hole Transport Layer Using Time Resolved Photoemission*, *The Journal of Physical Chemistry C* **124**, 3873-3880 (2020).
- [31] A. K.-V. S. W. G. Alexander V. Naumkin and J. P. Cedric, *NIST X-ray Photoelectron Spectroscopy Database*, Measurement Services Division of the National Institute of Standards and Technology (NIST) **20899**, 20899-20899 (2012).

- [32] A. Chu, B. Martinez, S. Ferré, V. Noguier, C. Gréboval, C. Livache, J. Qu, Y. Prado, N. Casaretto, N. Goubet, H. Cruguel, L. Dudy, M. G. Silly, G. Vincent and E. Lhuillier, *HgTe Nanocrystals for SWIR Detection and Their Integration up to the Focal Plane Array*, ACS Applied Materials & Interfaces **11**, 33116-33123 (2019).
- [33] A. Chu, C. Gréboval, N. Goubet, B. Martinez, C. Livache, J. Qu, P. Rastogi, F. A. Bresciani, Y. Prado, S. Suffit, S. Ithurria, G. Vincent and E. Lhuillier, *Near Unity Absorption in Nanocrystal Based Short Wave Infrared Photodetectors Using Guided Mode Resonators*, ACS Photonics **6**, 2553-2561 (2019).